*Preprint of paper published as J. Phys. D: Appl. Phys. 47 (2014) 224018*

# Multiscale modelling of plasma-wall interactions in fusion reactor conditions

**K Nordlund, C Björkas, T Ahlgren, A Lasa, and A E Sand**

EURATOM/Tekes, Department of Physics, P.O. Box 43, FI-00014 University of Helsinki, Finland

E-mail: kai.nordlund@helsinki.fi

**Abstract.** The interaction of a fusion reactor plasma with the first wall materials involves a complex multitude of interlinked physical and chemical effects. Hence modern theoretical treatment of it relies to a large extent on multiscale modelling, i.e. using different kinds of simulation approaches suitable for different length and time scales in connection with each other. In this Review article, we overview briefly the physics and chemistry of plasma-wall interactions in tokamak-like fusion reactors, and present some of the most commonly used materials simulation approaches relevant for the topic. We also give summaries of recent multiscale modelling studies of the effects of a fusion plasma on the first wall materials modification, especially on swift chemical sputtering, mixed material formation and hydrogen isotope retention in tungsten.

PACS numbers: 28.52.Av, 28.52.Fa, 34.20.Cf

Submitted to: *J. Phys D: Appl. Phys*

## 1. Introduction

In tokamak-like fusion reactors [1, 2] intended for practical power production, the plasma confinement is not – and should not be – perfect. Since the D+T nuclear fusion reaction produces He, which no longer undergoes fusion at a meaningful rate, this He needs to be pumped out from the reactor. All modern tokamak-like reactors are hence designed to have a *divertor* at the bottom of the reactor, where the He is pumped out, see Fig. 1 (it is also possible to have another divertor at the top in a so called double-null configuration, implemented at least in the EAST tokamak [3]). The plasma properties are such that the divertor is subject to a considerably high (of the order of $10^{20}$ ions/cm$^2$s) flux of H isotopes with energies of the order of 1 - 100 eV. Some leakage occurs also at much lower fluxes at the main wall, but the energy of the impinging particles can be much higher, up to the order of 1 MeV [4]. Hence the plasma-facing parts of the first wall are exposed to continuous irradiation by energetic ions and neutral atoms. The whole reactor is at the same time also subject to neutron irradiation that damages the materials [5, 6] but discussion of this topic, although very interesting, is outside the scope of this article.

The effects of energetic ion irradiation on materials have been extensively studied for more than a hundred years [7, 8] due to their relevance for Rutherford scattering [9, 10], ion beam analysis [11], thin film production [12, 13, 14], semiconductor technology[15, 16] and most recently the possibility to synthesize and modify nanomaterials with them [17], just to name a few examples.

Due to the long and extensive study of the effects of radiation on materials, it is known that the irradiation can lead to a large variety of outcomes on the material depending on ion species, energy and incoming angle as well as the type and temperature of the irradiated material. The initial stage of materials modification is known as a collision cascade, and its basic physics is illustrated in Fig. 2. Many of the known effects resulting from single and multiple cascades are summarized schematically in Fig. 3. The figure illustrates that the effects which can occur are complex, and understanding them requires a very good understanding of both the penetration mechanisms of energetic particles (essentially a variety of nuclear physics) and materials physics and chemistry.

All of the effects shown in Fig. 3 can occur in fusion reactors, although some are more likely than others, depending on the design. For instance, in a reactor consisting of only metal parts, amorphous zones do not form (pure elemental metals cannot be amorphised [21]) except possibly in metal alloys that may have formed due to erosion, transport and redeposition. Other effects such as sputtering of the wall material [50], blistering [51] and tritium retention [52, 53] can be very serious problems and possibly even showstoppers for the design of commercially viable fusion power plants. Hence understanding of the plasma-wall irradiation in fusion reactors requires a good understanding of relevant ion irradiation effects on materials.

Fusion reactors are, however, even more complex than a typical ion irradiation setup based on an accelerator, as sputtering of materials from the first wall can change the plasma properties [54, 50], which in turn can change the surface irradiation conditions. Hence

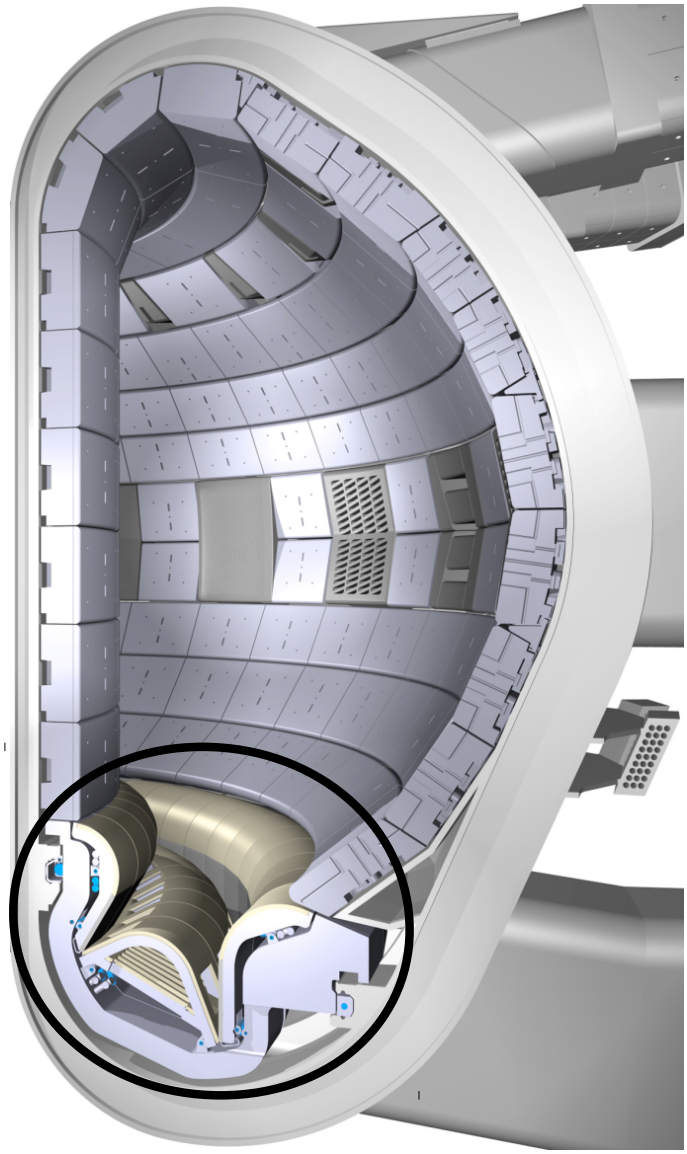

**Figure 1.** Cross section of the ITER [2] tokamak design. The black circle at the bottom shows the divertor region. In the current official design of ITER; the divertor plasma-facing parts are composed of C and W, and the main wall is lined with Be. However, very recently the scientific advisory committee of ITER recommended leaving out the carbon completely for cost-saving purposes [18].

the total process is a complex feedback process, and full description requires a combined materials and plasma simulation approach. Ultimately, a too high erosion of heavy (high-Z) particles into the core plasma can cool it down and extinguish it [2], which of course means that for power-plant operation the erosion must be well controlled. In this Review we do, however, focus on reviewing the science of the plasma-material interaction itself, as this already offers a fascinatingly complex and challenging field of study.

As figure 3 illustrates, the physics and chemistry of plasma-wall interactions is

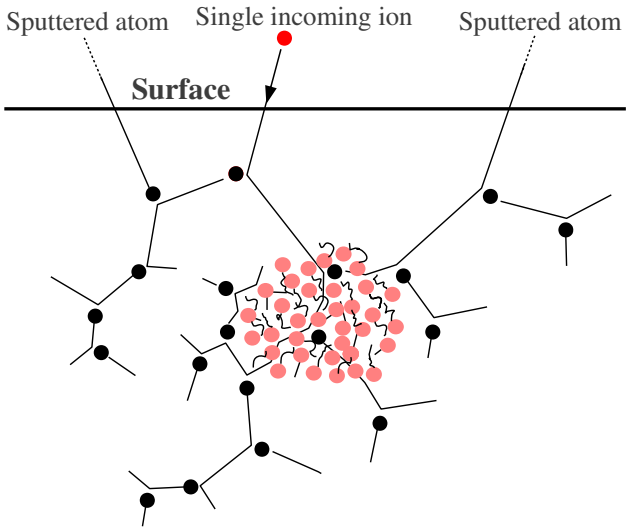


**Figure 2.** Illustration of the physics of collision cascades. At high kinetic energies ($\gtrsim 1$ keV) an incoming ion and the recoils (black) collide only occasionally and travel in almost straight paths between the collisions. They lose energy during the collision and continuously to electronic friction. This phase, which can be described by the binary collision approximation (BCA) method, leads primarily to point defect production and single atom sputtering. When they have slowed down sufficiently, a dense region of many-body collisions known as a heat spike can form [19, 20, 21]. In such regions complex damage such as dislocations [22] and craters [23, 24] can form.

complicated and encompasses more than 10 orders of magnitude in time and length scales. The initial ballistic collisions between atoms occur on femtosecond time scales [21], while for instance ripple and fuzz formation can take seconds or minutes to become significant [37, 48]. Similarly, even though a single high-energy collision involves impact parameters of the order of 1 Å [55], the size of blisters can be tens of microns [42] and strain effects can cause bending of macroscopic Si wafers [56]. Hence no single materials modelling tool can be used to examine all aspects of plasma-wall interactions, and it is natural that multiscale modelling methods have been taken into use to examine them. The concept of how different multiscale simulation methods can be used to model different length and time scales is illustrated in general in Fig. 4, and also the range that is relevant to the international ITER reactor, currently under construction in the EU, is shown. In a power-plant scale reactor (the first of which is known as DEMO in the current fusion roadmaps) the operation times would be so long that the whole time range would be relevant.

In this Review, our aim is to provide an overview of multiscale modelling methods of relevance to fusion plasma-wall interaction modelling, and provide representative recent examples of their use. We do not, however, attempt to provide a comprehensive review of all modelling work on plasma-wall interactions in fusion, as the entire literature is much larger than what can be included in a relatively concise topical review like the current one. The rest of the Review is organized as follows. In the subsections of Section 2 we present

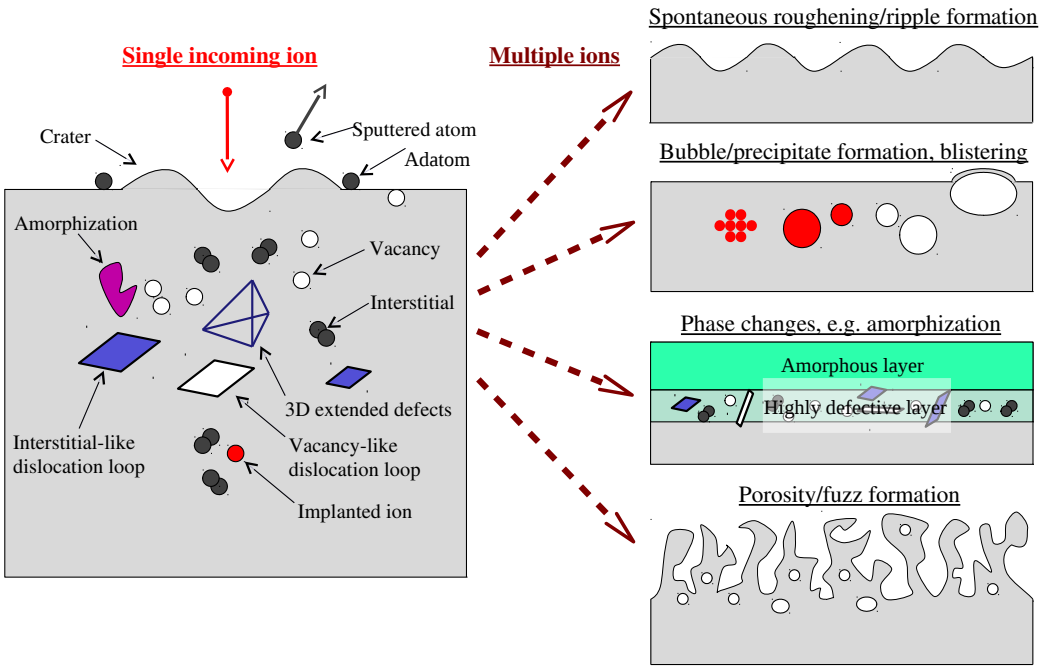


**Figure 3.** Schematic representation of physical effects that can occur during ion irradiation of materials. Note that a single kind of ion irradiation on the same material cannot lead to all these effects, but this illustration shows possible effects that are known to occur for some ions on some materials. The left side shows effects known to occur when a single ion irradiates a material. These include sputtering (atom erosion due to the high energy of the impacting particle) [7, 25, 26], production of point defects [21], cratering [27, 28], implantation [29], and direct formation of extended defects such as dislocations [30, 31], stacking fault tetrahedra [32, 33, 34] and amorphous regions [35, 36]. For prolonged irradiation, i.e. when multiple ions impact on the same region of material, several additional effects can results from the damage buildup. Right, top: prolonged irradiation can for certain incidence angles and materials lead to surface nanostructuring in ripple-like forms [37]. Right, second from top: buildup of the implanted ions can lead to formation of precipitates (nanoclusters) and [38, 39], bubble formation [40, 41], which can eventually lead to blisters on the surface [42]. Right, third from top: especially in semiconductors and insulators, radiation can lead to the formation of a continuous amorphous region [43, 44, 45, 46]. Right, bottom: some materials such as Ge and W form a highly porous surface layer after prolonged irradiation with certain ions [47, 48, 49] – the case of He irradiation in W is now considered a serious issue for fusion reactors.

briefly the physical principles of the most commonly used methods in current irradiation materials science, comment on their relevance to fusion plasma modelling, and provide references for readers wanting deeper information. In section 3 we describe the swift chemical sputtering mechanism that has proven to be highly relevant specifically for fusion plasma-wall interactions. In section 4 we discuss the formation of mixed materials, which is a serious issue in reactors due to redistribution of plasma impurities. Finally in section 5 we discuss how atomistic simulations tools can be combined with rate equations to model H behaviour in reactor W on macroscopic timescales.

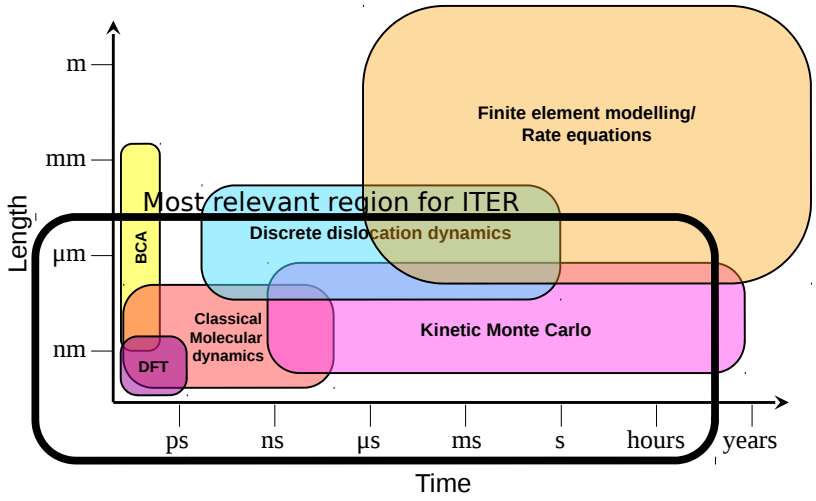


**Figure 4.** Rough description of the approximate time and length scales that can be handled with some of the most common materials simulation methods in general. The inner box emphasises the point that since ITER won't be a continuously running machine, with respect to radiation effects there won't be a total damage buildup time that would be of the some order as the years relevant to fission and fusion power plants. For the same reason it is unlikely the damage effects would build up to macroscopic length scales. BCA is an abbreviation for binary collision approximation and DFT for density-functional theory. All the methods are described at length in the main text.

## 2. Multiscale modelling

### *2.1. Density-functional theory (DFT)*

The density-functional theory (DFT) approach [57, 58] is based on two theorems by Hohenberg, Kohn and Sham, which state that (1) the ground state energy of a non-degenerate electronic state is a unique functional of its density and (2) the energy can be obtained by variation of the universal density functional with respect to the charge density. This implies that calculation of the wavefunction of a many-electron system is not required in order to find the total energy, but that it is enough to know only the charge density. This leads to a major reduction of the computational complexity compared to solving the true all-electron Schrödinger equation. However, the exact density functional is not known, and many different approximate functionals are used instead. Often these are chosen based on what compares best to experiments, and thus DFT is not necessarily a fully *ab initio* method in the sense of using no empirical input.

DFT-based and other quantum mechanical methods have a high accuracy but are computationally very expensive; simulations are normally limited to systems composed of a few hundred atoms and picosecond time scales (cf. Fig. 4). This makes the use of such methods impractical for tackling most radiation-related problems, e.g., formation of defects in collision cascades or direct dynamical simulations of defect diffusion. However, in some limited low-energy cases, direct quantum mechanical simulation of radiation-induced defect

production has been achieved [59, 60, 61]. More commonly DFT is used to obtain the energies and diffusion behaviour of defects (for a few examples in different classes of materials see e.g. [62, 63, 64, 65, 66, 67, 68, 69, 70, 71, 72]), which can be very useful for examining H and He behaviour in fusion reactor materials . An example of such usage is given in section 5.

### *2.2. Binary-collision approximation (BCA)*

The binary collision approximation is the oldest computer simulation approach for calculating the passage of ions in solids [55, 73]. In this approach, the passage of an ion in a material (solid, liquid or gas) is calculated as a sequence of independent binary collisions by solving the classical scattering integral for purely repulsive interatomic potentials [55, 74]. The BCA code TRIM/SRIM [75, 76, 77] is widely used in the ion irradiation field due to its convenient graphical user interface and extensive database of electronic stopping powers. It (as well as most BCA codes developed specifically for fusion simulations [78, 79]) uses a random ("Monte Carlo") algorithm to select the impact parameter of the next colliding atom as well as its type. The solution of the integrals of motion results in precise scattering angles for both the projectile and the target atom. Hence it can describe fairly accurately amorphous materials. Some BCA codes can also describe crystals, such as MARLOWE [55, 80] and "Crystal-TRIM" [81].

The BCA method has several limitations. It is not able to distinguish when a cascade goes over from the linear cascade to the heat spike regime, but keeps treating the collisions as independent binary collisions regardless of the collision density. Because of this, its range of physical validity for single ions is limited to sub-ps timescales (cf. Fig. 4). Although it can be used to estimate damage production (basically by counting recoils that exceed the threshold displacement energy) [82], it cannot tell anything about the atomic structure of these defects. The description of sputtering or other surface effects (important in nanosystems) is problematic as the inherent algorithm does not have a unique way of describing the atom binding at surfaces [83, 84]. Nevertheless, BCA often gives reasonable deposited energy and range distributions and primary recoil spectra for a wide range of materials [85, 86, 87, 88, 79, 89, 90, 91], and it is orders of magnitude more efficient than molecular dynamics simulation.

Due to its efficiency, the BCA method is of particular interest for the fusion community because of at least two reasons: it can be coupled concurrently with plasma simulation codes such as ERO [92], and it can (together with appropriate statistics-collecting algorithms) be used to track material mixing due to ion implantation and surface composition change due to preferential sputtering. The BCA code TRIDYN [78] was developed particularly for simulating composition changes as a function of depth [86, 93, 94], and its successor code SDTrimSP [95] can do this also as a function of lateral surface position and height.

### *2.3. Molecular dynamics (MD)*

In molecular dynamics (MD), Newton's equations of motion are numerically solved to determine the time evolution of a system of interacting objects [96, 97]. It is a very widely

used method to study all kinds of atomic-level physics, chemistry and biological issues [98, 99], and by no means specific to radiation effects. For simulation of radiation effects, the basic MD methods [96] need to be amended with a few solutions specific to radiation effects. These include accounting for electronic stopping as a frictional force [100], joining the equilibrium interatomic potentials with realistic high energy repulsive interactions[75], and making the time step adaptive to the maximum kinetic energy and force in the system in the ballistic phase of the cascade [100] while reducing it to a normal constant equilibrium time step after the cascade. Also, the radiation effect simulations cannot be carried out in any thermodynamic equilibrium ensemble as the initial collisional stage is not a thermodynamic system at all because the collisions occur faster than the relaxation time of the solid. Hence typically the central part of the system is treated with direct solution of Newton's equations of motion, while the boundary regions far from the collision zone are cooled down to remove the excess energy introduced in the system [101, 17].

MD is very well suited to examine the nuclear collision and heat spike aspects (cf. Fig. 2) of primary radiation damage, as with current computers it is possible to simulate the entire extent of collision cascade evolution both in space (up to length scales of hundreds of nanometers in three dimensions) and time (up to nanoseconds) [102]. MD simulations require the forces as the starting point for solving the equations of motion. The forces can be obtained directly from DFT or with classical interatomic potentials. As DFT MD simulations are still limited to a few hundreds of atoms [61], classical (empirical, analytical) potentials remain the method of choice for high-energy radiation effect simulations, as these typically involve at least tens of thousands of atoms.

Potentials exist for a wide range of systems and purposes. However, when simulating radiation effects, it is crucial to select potentials that allow for bond breaking and reformation, ruling out the use of most molecular mechanics force fields [98]. For carbon-based systems, the Brenner potential [103] and its extensions [104, 105] as well as the ReaxFF formalism [106] allow for bond breaking. The Brenner potential has proven to be quite useful for modelling effects of fusion reactor hydrogen isotopes impacting on carbon-based reactor materials [107, 108, 109, 60, 110, 111, 112, 113, 114, 115], as will be discussed further in section 3.1.

For metals, the Finnis-Sinclair and embedded-atom method potentials and their functional equivalents are widely used, [116, 117, 118, 119, 120] while for covalently bonded materials Tersoff-like bond order potentials [121, 103, 122] have proven to be quite successful. For compounds of different types of materials, far fewer potentials are available, but since the Tersoff and Finnis-Sinclair-like potentials are fundamentally similar [103, 123], a Tersoff-like formalism has proven to be useful in development of potentials for carbides, oxides and nitrides.[123, 124, 125, 126, 127].

To enable fusion-reactor plasma-wall interaction modelling in an ITER-like environment involving Be, W and possibly also C, interatomic potentials for the entire Be-W-C-H quaternary system in the Tersoff-like potential formalism [126, 128, 129] have been developed, using the well-tested Brenner potential for C-H [103] as a basis. Specifics of this potential will be discussed in section 4.2.1. Later specific potentials better optimized for

W and W-H have been added to the list of ITER-relevant potentials [130, 131].

### *2.4. Kinetic Monte Carlo (KMC)*

The main limitation of MD is the time scale. The MD time step is of the order of 1 fs, and cannot be increased in a general non-equilibrium situation. For systems involving well-defined transitions from one state to another, several speedup schemes exist [132, 133, 134], however, these do not generally work well in amorphous materials. This limits most MD simulations to nanosecond time scales. As a direct consequence, most diffusion and other long-time scale evolution processes are not accessible by MD.

Kinetic Monte Carlo (KMC) methods can sometimes solve this problem [135, 136, 137, 138]. The method takes as input the rates of relevant processes in a system, which typically are the defect migration rates and flux of incoming ions, and simulates the time evolution of the atoms or objects. The algorithm selects the processes proportional to their rates, so no computational capacity is lost in time steps with no events occurring.

The time in KMC advances stochastically, but on average as $\Delta t = 1/R$ where $R$ is the sum of all rates $r_i$ in the system. Hence if fast-moving objects vanish from the simulation due to e.g. recombination, the high values of $r_i$ vanish from the sum $R = \sum r_i$. This makes R decrease and hence the time advancement $\Delta t$ increase. Thus a KMC simulation may speed up in the evolvement of real time as a system develops, which is a major advantage to simulations.

There are many varieties of KMC. In atomic kinetic Monte Carlo (AKMC) simulations all atom coordinates are included but only one or a few defects (typically vacancies) at a time are moving [139]. In other modifications of the method, only the mobile defects are followed, and the lattice atoms are not explicitly described at all (such methods are known as object, reaction, event, or first-passage kinetic Monte Carlo, i.e. OKMC [140, 141], RKMC, EKMC [142] or FPKMC [143], respectively). Since only the objects of interest are simulated, this allows for simulation of macroscopic time (up to several hours) and length scales.

KMC simulations have been used to examine many aspects of hydrogen diffusion in fusion first wall-relevant conditions, especially for carbon-based materials [144, 145, 146] and W [147, 139, 141, 148]. We consider it likely that the use of different varieties of this group of methods will further increase as knowledge of the defect diffusion properties needed as the input for KMC keeps increasing.

### *2.5. Discrete dislocation dynamics (DDD)*

Discrete dislocation dynamics aims to model the behaviour of dislocations [149, 150] by describing a dislocation line as a sequence of connected line segments. These line segments interact with each other via their strain fields, which for isotropic materials are known analytically [150]. Taking into account crystal anisotropy is challenging, but advances have been made towards this goal recently [151, 152]. Once the interaction strength is known, the motion of dislocations is solved with the same basic principle as atom motion is solved in MD. The segments are given a fictitious mass that gives them reasonable velocities compared to experimental observations.

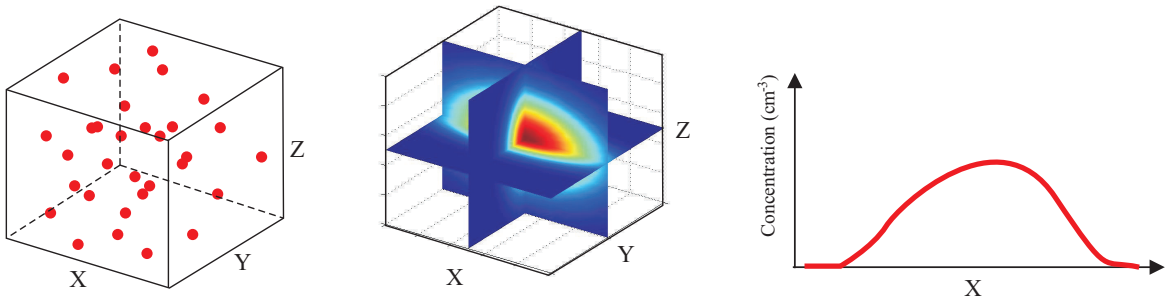


**Figure 5.** In RE, the positions of the wanted entities are represented as concentration profiles. Usually, only solution in one dimension is needed.

DDD is in principle a very powerful tool to predict the mechanical response of materials (especially metals where dislocation dominate the mechanical behaviour on the macroscopic scale) to external deformation, and some studies have given insight of plastic behaviour of materials [153]. Unfortunately the knowledge of dislocation reactions and formation mechanisms needed to parametrize DDD is incomplete. Hence currently there are extensive activities ongoing to use MD modelling to determine dislocation reactions that can be used to develop the DDD methods further, see e.g. [154, 155, 156, 157].

DDD is not likely of major relevance for plasma-wall interactions in ITER, as the total radiation doses there are not high enough to induce major mechanical property changes in the W. However, at the DEMO/power plant stage, major materials modification at the divertor is expected due to the combined ion and neutron fluxes [148], and also DDD will likely get into use for plasma-wall interaction modelling.

### *2.6. Rate equations (RE)*

To be able to simulate long time (seconds to years) and large volume (corresponding to $> 10^{15}$ atoms) processes, so called rate equations (RE), also called *rate theory* can be used. The RE formalism comes from the *Continuity Equation*, *Transition State Theory* [158, 159] and the *Theory of sink strengths* [160, 161]. The positions of the considered defects, atoms or impurities are transformed to concentration distributions, see Fig. (5), and these are solved numerically. Note that the inputs to RE modelling are from a physical point of view essentially the same as those for KMC (albeit used in a different form). As RE are a fully continuum method, they have the advantage that they can treat fully macroscopic time and length scales, at least for 1D profiles. To simulate a system with 3D information stored of the system state, also rate equations become computationally challenging.

The number of atoms vs. simulation time for different simulation methods are summarized in Fig. 4, but note that the rapid increase in computational capacity changes this estimation continuously. Section 5 gives an example of the use of rate equations for fusion modelling.

### *2.7. Finite-Element Modelling (FEM)*

The basic idea of finite-element modelling (FEM) of materials is to describe an object of arbitrary size as a set of connected triangles (2D) or prisms (3D). The size of these prisms can change based on an external mechanical load in a way that is consistent with the elastic constants of a material. In its basic implementation, FEM can simulate elastic deformation of materials, both for isotropic and anisotropic materials, and can for known elastic constants achieve an arbitrarily accurate solution of the elastic deformation. The size of the prisms can be widely varying in different regions of space and there is no inherent limit to what their size can be, which makes FEM well suited to study macroscopic objects. Moreover, with algorithmic extensions and proper parametrization from experiments or lower-level methods, FEM can be extended to also describe plastic deformation [162, 163].

The major limit of FEM is that it does not have any information of atoms, although it is possible to make a multiscale combination of FEM and atomic simulations like MD [164, 165, 166].

FEM is very widely used to examine mechanical properties of macroscopic objects, and is a standard tool in the materials manufacturing industry. In this respect, the design of the entire ITER reactor is strongly dependent on FEM, and it can also be used to model e.g. the change of the mechanical size of the divertor components due to thermal expansion under the heat cycling of ITER. Since the heat is coming from particles (electrons, ions and light) escaping the plasma, in one way FEM modelling is also relevant to fusion plasma-wall interactions. In the more focused sense of this article of considering materials damage by plasmas, FEM is also relevant for modelling the macroscopic behaviour if the changes of the mechanical properties by radiation are taken into account in a FEM model. However, as noted above for DDD, ITER is not likely to be subject to major changes of the mechanical response, and hence the radiation damage plasma-wall relevance of FEM will be more significant at the DEMO/power plant stage.

## 3. Swift chemical sputtering

### *3.1. Carbon and other covalently bonded materials*

The bombardment of carbon-based materials by low-energy (1-100 eV) H isotopes (H, D or T) is still of great interest in nuclear fusion reactors, since carbon composites were for a long time considered the materials of choice for the reactor first wall, are still used in several existing reactors such as JT-60 [167], and will be used in future machines such as the Wendelstein-7X stellerator [168]. Carbon in different graphitic forms has several advantages for fusion, such as a very good thermal stability up to high temperatures, relatively low cost, and low atomic number $Z$ (impurities in the main fusion plasma cool it down as $Z^2$ – $Z^4$ depending on which process is considered). Experiments have shown that the lowest part of the reactor, the divertor, is eroded by the incoming H due to sputtering of hydrocarbon molecules [169, 170, 171, 172, 173, 174, 175, 176]. The mechanism behind this effect was long unclear [177, 173] since at the lowest energies (1 - 10 eV) physical sputtering of the wall

is impossible.

At high temperatures it is known that H atoms can enter the amorphous hydrogenated carbon (a-C:H) samples and change locally the bonding structure, resulting in the formation of a weakly bound molecule which can migrate to the surface and desorb [54]. This requires thermal activation, however, and hence it cannot explain the observation that the desorption rate is the same between liquid nitrogen and room temperature [178].

Using MD simulations of the bombardment process, a new kind of chemical sputtering mechanism which can lead to instantaneous erosion of hydrocarbon species from surfaces has been discovered [107, 108, 109, 60]. The nature of the mechanism is easiest to understand by considering the model system of one H atom colliding with a C-C dimer. The most symmetric case possible is the one where the H atom moves perpendicular to the chemical bond towards the middle of it, see Fig. 6. The momentum transfer in the $y$ direction can be calculated [60] as

$$p_y = \int_{-\infty}^{\infty} f_y(t, E_{kin}^H) dt \approx \bar{f}_y \bar{\tau}, \tag{1}$$

where $f_y$ is the force acting on the carbon atoms and $E_{kin}^H$ the initial kinetic energy of the H atom. To enable easier understanding, the integral is simplified to be a product $\bar{f}_y \bar{\tau}$, where $\bar{f}_y$ is an effective average force during the collision, and $\bar{\tau}$ an effective average time the H atom spends in the area of the C-C bond.

If the kinetic energy of the H ion $E_{kin}^H$ is low, the H atom returns back without entering the region between the C atoms. Then $\bar{f}_y$ and the $y$ momentum are small and the bond is not broken (Fig. 6 top). When the initial kinetic energy of the impinging particle is high enough for the H atom to stay for a (relatively) long time $\bar{\tau}$ in the region between the atoms, the bond breaks (Fig. 6 middle). If the initial kinetic energy is even higher, the bond breaking ceases (Fig. 6 bottom). This is because, although $\bar{f}_y$ is large, the particle spends too little time between the carbon atoms to cause any bond breaking ( $\bar{\tau}$ is short). Thus there is a finite energy window in which the bond breaking can occur. The characteristic time of this process is very short, of the order of 10 fs. Because the mechanism involves atom bonding, requires kinetic energy and is rapid, it was named “swift chemical sputtering” [179].

To rule out the possibility that the mechanism would be an artifact of a particular interatomic potential, it has been shown that the effect occurs as described above using three varieties of the Brenner potential [103, 105, 104], as well as in a tight-binding quantum mechanical framework which is completely independent of the classical simulations [60]. This model system was also examined with He, and found that also it can lead to bond breaking, albeit with a clearly lower cross section.

In addition to the study of the dimer model system, extensive simulations of H, D and T bombardment of actual a-C:H material have been carried out. The main results obtained can be summarized as follows. It was shown that the swift chemical sputtering (SCS) mechanism leads to sputtering of small hydrocarbon molecules down to energies of about 2 eV, and that the sputtering yields obtained are in the experimental range of yields [109, 110]. It was also observed that the sputtering yields are highly sensitive to the detailed surface structure [180],

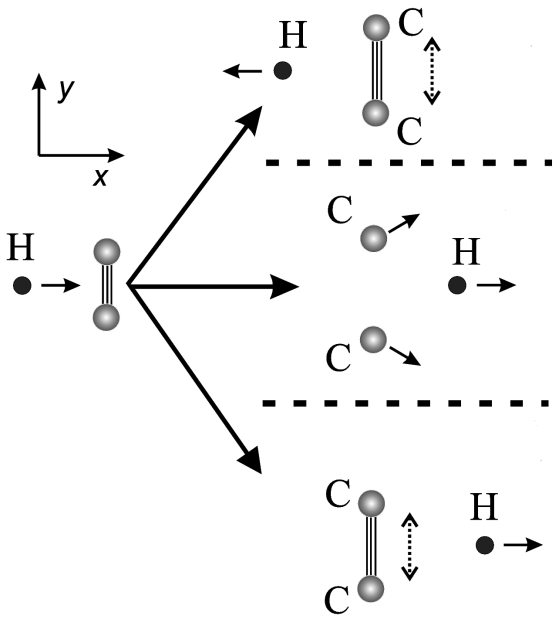


**Figure 6.** Schematic representation of the swift chemical bond breaking in a carbon dimer. Depending on the energy three different outcomes are possible. Top right: incoming energy too low, hydrogen does not penetrate bond, no bond breaking. Middle right: suitable energy, hydrogen penetrates bond and slows down so much there is sufficient time for bond breaking. Bottom right: hydrogen penetrates bond rapidly, there is not sufficient time for momentum transfer, and bond does not break. Adapted from Ref. [60].

and that for high fluxes a H supersaturation can form on the surface, which can reduce the C sputtering by an order of magnitude [107]. These observations explain experimental results on the same systems. The temperature dependence of the sputtering yield was also examined, offering a possible explanation to why the yield had a maximum at about 700-900 K [109] (although the so called Küppers cycle [54] is certainly also active at these high temperatures). Most recently, we have found that even if 10% of the bombarding particles are He, Ne or Ar, with the *same* energy as the incoming H, the erosion yield does not change appreciably (more than $\sim$ 10 %) compared to the case of bombardment with H only [181].

Several groups have carried out similar simulations of H bombardment of carbon-based materials and found essentially the same mechanism to be active [111, 112, 113]. These simulations have also revealed several other aspects of the SCS mechanism carbon, such as its angular dependence [112], effect of electronically excited states [114], cobombardment with plasma impurities [115], high-flux effects [182], isotope effects [183], as well as the effect of sample structure [111]. The simulated yields have also been found to be in good agreement with experiments [110, 113].

Also the effect of doping carbon materials with other elements on the sputtering have been studied [184, 185]. For instance, several studies showed that Si concentrations around (5 – 10 at.%) reduce chemical sputtering yields by a factor of 2 – 3 compared to pure graphite [186, 187, 188, 189]. This effect was qualitatively reproduced in MD simulations [190].

Although reduction of the swift chemical sputtering carbon erosion yield is thus possible, the effect is essentially impossible to avoid for covalently bonded materials as it only requires a single H isotope of suitable energy to penetrate between two carbon atoms. This leads to the fact that any carbon-containing reactor will always suffer some erosion in the form of hydrocarbons. These can drift elsewhere in the reactor and redeposit, leading to the buildup of tritium-containing thin films [93] which are very difficult to remove, and can lead to the legal limits for tritium inventory to be exceeded [50, 53, 191]. This is the reason why carbon is not considered to be used in the D+T phase of ITER.

All of this work focused on carbon due to its importance in fusion reactors. Since our argument for how the bond breaking occurs is a very generic one and the time-dependent bond breaking argument is in no way specific to carbon, however, it is reasonable to assume that it might also occur in other covalently bonded materials. As a test case, Si was considered, and it was shown that it does, indeed, also sputter by the same mechanism [192].

### *3.2. Metals*

*3.2.1. Dimer model applied to metals* Since SCS involves bond breaking, the authors finding it, originally believed that it is natural only to covalent materials and that it would not occur in metals due to their non-directional bonding [192]. Later, the same authors found that applying the dimer model described above to the Be dimer, a similar bond-breaking occurs [193, 194], indicating that SCS also could be present in the metal Be. (A bond in metals is here defined as the attraction between lattice atoms.) The difference compared to the C dimer breaking lies only in the lower required energy, due to the different bond strengths. Even the mixed Be-W and Be-C dimers are seen to break when a H isotope penetrates in between the atoms. Bond breaking for a pure W material is, on the other hand, highly unlikely due to large mass differences between the H and W atoms and related weak momentum transfer [193, 195].

A real surface is naturally much different from a collection of dimers. For instance, the coordination number $Z$ of atoms located at the surface changes during irradiation (in the case of Be, it could range from only 1 to the ideal surface coordination $Z = 9$ or bulk hcp $Z = 12$), atoms can be manifold connected to not only other substrate atoms but also to added plasma or impurity atoms. Hydrocarbon chains are common on hydrogenated carbon surfaces, sub surface bubbles can form and the surface can be depleted on substrate atoms if the incoming ion flux is very high. All of this affects the ability of the substrate atom to be sputtered and a break-up during the simple dimer simulations does not therefore by default lead to actual Be sputtering through the SCS mechanism.

*3.2.2. MD simulations of chemical sputtering in Be* Moving from the dimer model to modelling a real surface irradiation event is possible by simulating bombardment of small surface slabs using MD (a typical cell contains a few thousand atoms). The simulations are done either cumulatively or non-cumulatively. The cumulative simulations are performed to mimic an evolving surface but due to extensive computational cost per impact, the flux and fluence of the incoming ions are usually restricted to a few thousand bombardments impacting

at a flux of $\sim 10^{28} m^{-2} s^{-1}$. A uniform bombardment of the surface is simulated by shifting the cell randomly in $x$ and $y$ directions ($z$ is defined as the surface coordinate and is non-periodic) before each impact and allowing the whole cell to relax at a chosen temperature in between. Fixing of the bottom atom layers keeps the cell in place and an infinite lattice is mimicked by keeping the cell borders at the desired temperatures at all times. Lengthy calculations are avoided when performing non-cumulative simulations. The surface evolution is then not of interest, but the focus is shifted to the interaction between a pure surface (alternatively a somehow prepared/modified or amorphous surface) and the irradiating species in an equilibrium situation. The two methods may give differing results, for instance when the impurity surface concentration plays a role [196].

Simulating D irradiation of Be surfaces reveals that SCS is indeed present in Be and furthermore an important erosion mechanism [197]. The release of BeD molecules already at low impacting ion energies, 7 eV, is the result.

Snapshots of a sputtering event where a 10 eV D ion is bombarding a Be surface is illustrated in Fig. 7. At the end, the incoming D ion is sputtered away as part of a $D_2$ molecule and an energy analysis shows that is has lost more than 90% of its initial kinetic energy. This loss of energy is a gain in potential energy of the Be atoms with which it interacts. Between figure A and B, the D ion collides with a Be atom, losing about 6 eV in the process. The rest of its kinetic energy is lost when it penetrates in between the Be atoms in C-E. In total, the D ion has caused five Be-Be bonds to break. Initially, four D ions were neighbours to the sputtered Be, but only one of these (number 2 in the snapshots) was sputtered together with the Be (a neighbour is defined as an atom being inside the cutoff range of the potential).

The top surface structure, or more precisely the neighbouring surroundings of a Be surface atom, is a highly important factor in the sputtering process. Since a 7 eV D ion is able to sputter a Be atom, the Be atom must be weakly bonded to the surface. This indicates that is has only a few bonds to other Be surface atoms. Example energies per bond in the above mentioned simulations for a surface Be atom with 9 Be neighbours are, on average, $0.30 \pm 0.01$ eV and with 6 Be neighbours $0.36 \pm 0.02$ eV. Calculating the same energies when a few D bonds are present results in: 9 Be and 2 D bonds = $0.25 \pm 0.01$ eV, 6 Be and 3 D bonds = $0.28 \pm 0.02$ eV [197]. At low bombarding energies, the amount of initial Be neighbours to sputtered Be atom is less than the amount in high energy cases where it reaches the ideal one of 9 of a hcp (0001) surface, which is explained by the larger penetration depths of the D ions at higher energies. Due to the same reason, the amount of D neighbours shows the opposite trend, meaning that the Be atoms in the low energy bombarding cases have a higher possibility to be weakly bonded to the surface and as such also to be easily eroded.

The mean release energy of BeD is around 2 eV, agreeing with observations that the molecules are released with much higher energy than that corresponding to the surface temperature [198]. Their release angles form a cosine distribution around the surface normal.

The chemical sputtering, here defined as the release of BeD molecules from the Be surfaces, is hence an essential factor in low energy bombardment regime. At 7-20 eV, the fraction of Be sputtered as BeD molecules (including $BeD_2$) can be as high as 100% (see Fig. 8). As the impact energy increases, Be atoms are released also via physical sputtering,

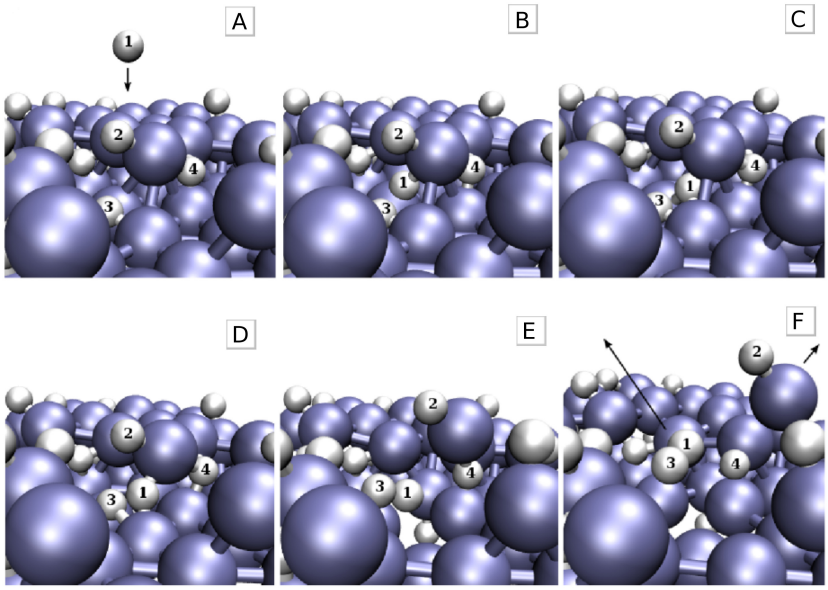


**Figure 7.** Snapshots at six different times during of a sputtering event. The D ions are represented by the small light gray spheres and the Be atoms are the larger dark spheres (colours on-line). The arrows in the last snapshot (F) show in which direction the sputtered $D_2$ and BeD molecules are moving.

lowering the BeD molecular fraction.

Performing non-cumulative simulations of D impacting on a pure Be surface would result in a much higher sputtering threshold than in the cumulative case [196]. This is due to the lack of D ions accumulated in the surface, meaning that all Be atoms are strongly bonded to the surface and therefore require relatively much kinetic energy to be released from the surface. Non-cumulative simulations using surfaces with added D (e.g. taking the final cell structure after cumulative bombardments), result in a more realistic threshold. Using cells corresponding to any real fusion reactor wall element or experimental sample would be ideal, however, parameters such as the structure of and D content in the samples are often difficult to quantify and therefore not well known.

BeD molecules are also released from BeW surfaces during MD simulations [194]. The addition of W in the surface makes the contribution of the chemical branch less prominent compared to pure Be surfaces, especially if the top layers are dominated by W, which could be a result of preferential sputtering of the lighter element Be.

*3.2.3. Experimental observations of BeD molecules* BeD molecules have also been observed during experiments, both in the linear plasma device PISCES-B [198] and in the TOKAMAK JET [199, 200]. In PISCES-B, the molecular release has been found to be dependent on the incoming D ion energy, showing a similar trend as in the MD simulations (see Fig. 8), but also on the surface temperature of the exposed Be sample. At high temperatures, the BeD spectroscopic signal, and hence the contribution to the sputtering coming from the

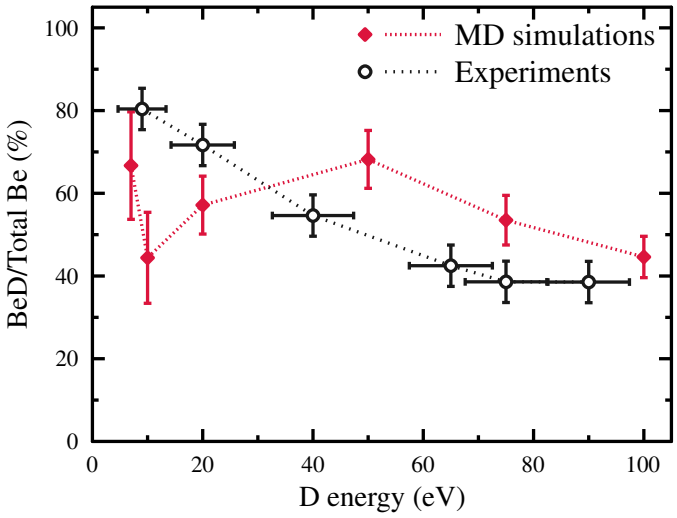


**Figure 8.** The fraction of Be sputtered as BeD molecules as a function of incoming D ion energy during MD simulations and measured in the PISCES-B facility [197].

molecules, is seen to decrease in comparison to lower temperatures. This has been related to the decomposition of $BeD_2$ molecules on the Be surface. After a peak at around 440 K, $D_2$ molecules are released from the beryllium hydride ones and therefore lower the chance of BeD release [198].

Recent observations in JET also support this temperature dependency [191]. When measuring the BeD signal from Be tiles in the first wall, a significant intensity drop is observed between surface temperatures of around 500 K and 700 K. Gas balance calculations revealed that the chemical sputtering contribution, i.e. the BeD molecular fraction of the total sputtering, was around 33% at 75 eV impact energies, which agrees well with both simulated and measured PISCES-B values.

*3.2.4. Multiscale modelling of Be irradiation experiments* Modeling efforts to tie the MD simulations and experimental observations of the BeD molecules together have been done by using the 3D plasma impurity code ERO [92, 201, 194, 202]. ERO follows particles that are either physically or chemically eroded from different surfaces of a fusion device due to impinging plasma ions (fuel or impurities). The released particles enter the plasma as neutrals but at each time step, the ionization (or dissociation) probability is calculated, which depends on the local plasma parameters (electron density and temperature) and calculated reaction rates. Once ionized, the movement of the ions is affected by the magnetic and electric fields. Also friction with the background plasma, thermal forces and diffusion are taken into account. The eroded particles can return to the surface and be reflected or cause additional sputtering or simply escape from the simulation volume.

The ERO code has been applied for modeling PISCES-B experiments aimed at

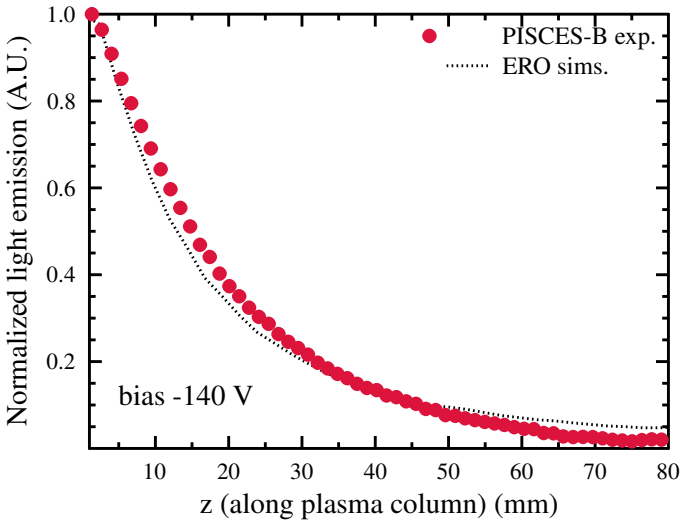


**Figure 9.** The normalized light emission intensity of the BeD band. The circles represent PISCES-B experimental results and the dotted line is simulated results. The target bias voltage was -140 V. The data is from Refs. [202, 194].

quantifying the Be and BeD appearance near a Be target exposed to a D plasma. The light emission from both neutral and ionized Be and the BeD band (497.3-499.2 nm) was spectroscopically measured and the plasma parameters (electron temperature and density) and target bias voltage were varied [202, 194]. The temperature of the target was not regulated.

MD data were used for determining the physical and chemical sputtering yield in the ERO simulations. Assuming that the contribution to the total sputtering from the BeD branch decreases from 100% at low impact energies to only around 20% at higher energies, resulted in an overestimation of the sputtering when compared to the experimental observations [202]. However, since the surface temperature of the Be target was allowed to vary throughout the experiments, the chemical branch did not follow the above trend obtained for a sample kept at constant temperature. Instead, it showed a constant fraction at all impact energies (applied bias voltages) of around 17%. Assuming this fraction in the simulations resulted in better agreement [194].

Both the simulated and the measured profile of neutral BeD light as a function of distance from the Be target in the PISCES-B device is shown in Fig. 9. The figure illustrates that the penetration of simulated BeD molecules in the plasma is only slightly smaller than what is observed. The small differences could be explained by an overestimation of the assumed ionization and/or dissociation rates. In addition, since no reaction rates for this is available, the ERO simulations did not include volumetric formation of BeD through endothermic reactions between $Be^+$ and D2 [198], which also could add to the differences.

## 4. Mixed material development

The material that is released into the fusion plasma as a consequence of the plasma-wall interactions, will mostly return to the wall and thus reduce the gross erosion. However, part of the eroded species may migrate long distances and upon redeposition form layers of co-deposits and so called mixed materials, whose composition and structure distinctly differ from the initial wall material. The co-deposits may contain, in addition to the different wall materials, also fuel atoms, i.e. hydrogen isotopes. The impact of these mixed materials on fuel retention and the possible increase of erosion and degradation of thermo-mechanical properties of such layers are issues that need to be addressed when assessing the life-time of a fusion reactor.

Simulations provide an insight into the formation of these mixed materials on atomic level and also give information about their erosion behaviour and retention capabilities.

### *4.1. The carbon-tungsten system*

Mixing of W and C results in either the carbide WC or the subcarbide $W_2C$. Which carbide is formed depends on the temperature, as annealing evaporated C on tungsten substrates at 970 K shows that $W_2C$ is the dominating phase, until it is converted into WC at 1270 K [203, 204].

Ina *et al.*[205] have studied 10 eV - 1 keV C bombardment of initially crystalline W surfaces using both MD and KMC in order to quantify the C deposition and reflection. At low energies, a C layer is seen to form on top of the W surface. At the highest energies, a mixed "hybridization layer" is formed, which, however, does not exhibit any crystallinity or particular ordering. A steady state condition with constant sputtering of the deposited C and bulk W atoms is reached for this mixed layer and its C sputtering is larger than that of the deposited C layer. Atomic scale roughness not included in the KMC calculation were the cause for different results concerning the C deposition modelled with MD and KMC.

The sputtering of WC layers due to hydrogen isotopes has been studied using MD simulations [206, 207, 208, 195]. WC is an interesting system due to the large atom size and mass difference of the constituents, and MD simulations of radiation of bulk WC showed that this leads to a major elemental asymmetry in the damage production [209, 206]. Hence it is not surprising that also the plasma-wall interactions show major elemental asymmetries. Cumulative bombardments of both crystalline and amorphous WC surfaces with deuterium showed that for all ion energies used (up to 1 keV), the erosion of tungsten is negligible which is equivalent to preferential sputtering of carbon leading to a buildup of W atoms in the surface [206, 207], agreeing with experimental findings [94].

Other findings from the simulations [206, 207, 208, 195] include the fact that the tungsten sputtering is not enhanced for WC surfaces compared to pure W ones. The C sputtering yield, on the other hand, are of the same order of magnitude for C and W terminated surfaces, but the former can be larger by as much as a factor of 4, since the carbon atoms in the first surface layer can react more easily with the incoming deuterium ions. Sputtering is seen at impact energies as low as 10 eV, indicating that chemical sputtering, through the swift chemical

sputtering mechanism, is present, at amounts similar to that of pure C surfaces. Furthermore, the initially crystalline surfaces are amorphized during the cumulative bombardments. This amorphization is most pronounced at D energies of 100 eV, where the D retention also is the largest. The retained D, of which 33-48% are bound as $D_2$ molecules in the sample, hence facilitates the amorphization. Non-cumulative bombardment of amorphous surfaces with different W content also showed preferential sputtering of C, but with a decreasing yield as the W content increases.

### *4.2. The carbon-beryllium system*

Only one intermediate phase of beryllium carbon has been reported [210]. This phase is the ionic $Be_2C$ cubic antifluorite structure, which can be described as carbon atoms occupying fcc sites and beryllium atoms forming a cubic sublattice inside. In this way, each C atom is surrounded by eight Be atoms.

The carbide phase has been observed to form during 5keV $C^+$ irradiation of clean Be surfaces [211, 204]. A high fluence is needed to reach the necessary stoichiometry for carbide formation, and as the fluence increases, elementary C is formed as an adlayer on the top of the carbide. The same behavior is also observed during MD simulations. Figure 10 illustrates a Be simulation cell bombarded with 1000 C ions with an impact energy of 20 eV. A few layers of $Be_2C$ are observed in the mixing region as well as amorphous C at the very top surface where the C concentration is high. The carbide is thus formed already on a pico-second time scale.

The carbon-beryllium system has been studied also from many other points of view. DFT calculations have suggested that beryllium carbide can form via Be diffusing into graphite, forming first an intercalated beryllium-carbon compoint, which then undergoes a phase transition to beryllium carbide [212]. Sang *et al.*have developed a multiscale particle-balance model for reaction-diffusion and hydrogen inventory modelling in porous mixed Be-W-C layers [213]. Combinations of such different kinds of models will certainly lead to increased understanding of mixed materials in fusion conditions.

*4.2.1. Potentials for mixed materials* The formation of areas of amorphous C on the surface of mixed BeC materials sets certain requirements on the interatomic potentials used to simulate sputtering by H isotopes from these materials. Incident ions with low kinetic energy have time to react chemically with surface atoms. While a Tersoff-type potential [121], originally developed for covalently bonded materials, can well be applied to mixed metallic-covalent systems [123] such as BeC, this potential does not capture the very particular chemical behaviour of hydrocarbon systems.

The Brenner potential, on the other hand, is developed specifically to model intramolecular chemical bonding in hydrocarbons [103]. Brenner used the functional form of the Tersoff potential as a starting point, and added terms to this which account for the forces that arise from the specific bonding behaviour of hydrocarbons.

Bond conjugation is seen in certain hydrocarbon systems, when assigning single or

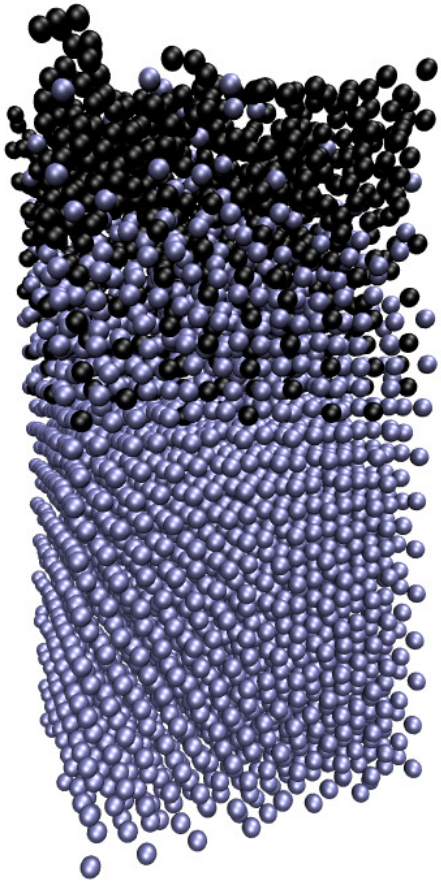

**Figure 10.** Structure of a Be cell bombarded with 20 eV C ions. $Be_2C$ layers are formed in the mixing region.

double character to bonds results in a chain of alternating single and double bonds between C atoms, such as in aromatic rings and graphene. In these configurations the C-C bonds actually share single and double bond character, and all are in fact of equal strength. On the other hand, situations arise where the nearest neighborhood of an atom pair is indistinguishable from the above configurations, yet neighboring single and double bonds do not have shared character, but are in fact clearly double and single, respectively. This behaviour depends on the atoms that the neighbors to the pair in question are bonded to. Thus, in order to determine whether a bond should be purely single or double, or mixed, a potential must take into consideration a larger area around a given bond.

The occurrence of free radicals is another special case arising in hydrocarbon systems which is not described by a calculation of bond strength based only on immediate neighbors. In this case a C atom does not share all its bonding electrons between its neighbors, but rather retains a high degree of reactivity, while at the same time the existing bonds are weaker than they would be if all electrons were involved.

Brenner's hydrocarbon potential accounts for these particular chemical effects by including terms dependent on the number and nature of second neighbors (*i.e.* neighbors

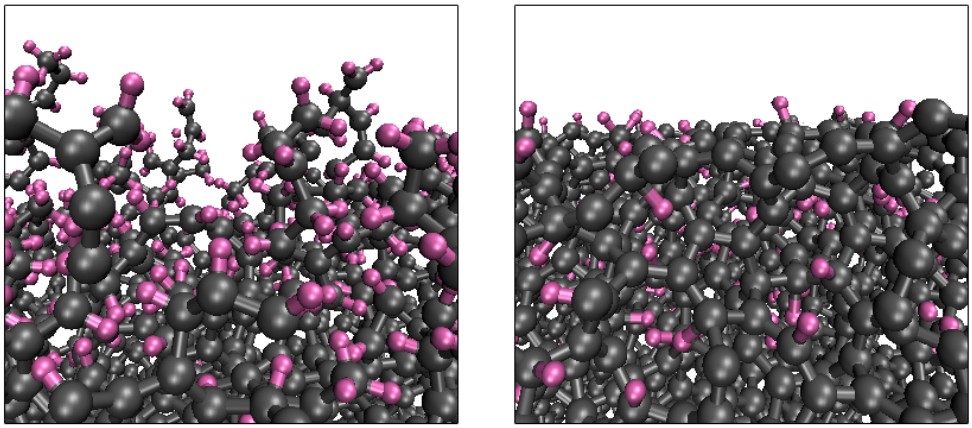

**Figure 11.** Amorphous C surfaces after 2000 consecutive D impacts. The picture to the right was simulated using a Tersoff-type potential, while to the left the Brenner hydrocarbon potential was used. Large (grey) spheres represent C atoms and smaller pink spheres represent D atoms.

of neighbors) to the pair whose bond is being calculated. The effect in low energy sputtering simulations is that carbon chains along the material surface more readily become hydrogenated, in comparison with the predictions of the pure Tersoff-type potential. This results in a substantial sputtering yield at low energies, which is consistent with experiment [214, 215]. The high yield is due to the formation of terminating methyl-like groups, which are the precursors to sputtered molecules [109]. Because of this the specific surface configuration of a sample has a large impact on the probability of chemical sputtering. Such terminating methyl groups are not formed in simulations with a Tersoff-type potential [216]. Figure 11 shows the difference in surface structure of an amorphous C surface after consecutive D bombardment with the two potentials.

*4.2.2. MD simulations of swift chemical sputtering in BeC* Surface evolution during D irradiation, captured by cumulative bombardments, is important in the BeC system due to the strong dependence on surface configuration of sputtering of the C component. This is especially true when the surface contains sizeable areas of amorphous C. In order to realistically capture the surface evolution in this case, the above mentioned chemical effects must be included. For this mixed metallic-covalent system, a viable solution utilizing current potentials is to simultaneously use both a Tersoff-type potential and the Brenner hydrocarbon potential. The calculation of a given bond then depends on which species are present among the atoms affecting the bond.

The analytical bond-order potential (ABOP) for the Be-C system [128] predicts the formation of areas of amorphous carbon and crystalline $Be_2C$, when a simulation cell containing excess C is annealed. In this way a realistic $Be_2C$ surface with an amorphous C

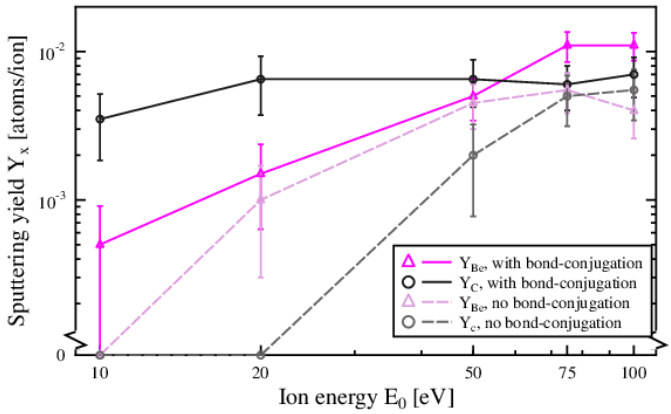


**Figure 12.** Sputtering yield from a mixed material surface with areas of $Be_2C$ and amorphous C, simulated with and without the bond-conjugation terms in the Brenner potential. [216]

area was created, and bombarded using the combined Be-C-D ABOP and Brenner potentials [216]. Comparison to simulations using only the Be-C-D ABOP show the importance of hydrocarbon chemical effects, especially when predicting the relative degree of sputtering of the different surface components. Simulations with the hybrid potential show a higher degree of C sputtering, and also the degree of molecular sputtering at lower energies was higher, as compared to yields obtained using the pure Tersoff-type potential. The sputtering yields for the two cases are shown in figure 12. For 10 - 50 eV ions chemical effects dominate, and C is sputtered preferentially over Be. Between 50 and 75 eV there is a turning point, when physical sputtering processes begin to dominate, so that above this the lighter element Be is sputtered preferentially, despite half of the simulated surface being composed of amorphous C.

## 5. To macroscopic timescales: H and He in W

### *5.1. H retention in W*

The refractory metal tungsten (W) has extraordinary physical and thermal properties and is intended to be used as a plasma facing component in the next step fusion device ITER. As a first wall material in ITER, W will be subjected to both low energy, high flux hydrogen (H) isotopes, and high energy neutrons that will create H trapping damage deep in the wall material. The H isotope retention should be kept as low as possible for both fusion efficiency and safety reasons. The natural and irradiation-induced traps will retain H isotopes and especially important is the tritium (T) retention. To understand the H retention in W, RE simulations above the displacement threshold energy $E_{th}$ are considered.

The simulated and experimental deuterium (D) retention in polycrystalline W at room temperature are compared. The D is implanted into W to a fluence of $5.8{\times}10^{20}$ D/m$^2$, with

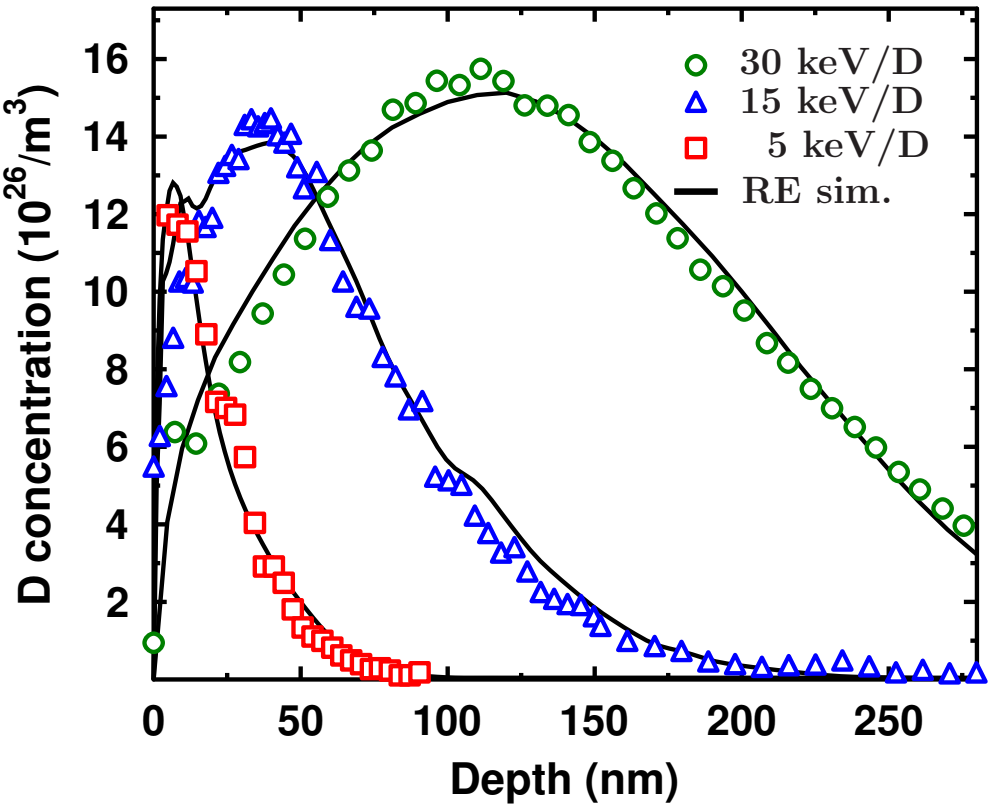


**Figure 13.** Experimental and simulated D distributions in W, with implantation energies of 5, 15, and 30 keV/D, to a fluence of $5.8\times10^{20}$ D/m$^2$.

three different implantation energies, 5, 15 and 30 keV/D, with a flux of about $3.2\times10^{17}$ D/m$^2$s. The main impurity, excluding Mo, in the W samples was carbon (C) $\sim$ 10$\mu$g/g, corresponding to about $10^{25}$ C atoms/m$^3$ (typical high purity 99.99% polycrystalline W by Plansee AG). The experimental details are described in [217] and RE details in [218].

An excellent agreement between the RE simulated, and all the 5, 15, and 30 keV/D experimental D concentration profiles was found, see Fig. 13. The fraction of the retained D, compared to the implanted fluence of $5.8\times10^{20}$ D/m$^2$, increases rapidly from about 8% to 35% as the implantation energy increases from 5 to 30 keV/D.

The final simulation outcome after irradiation is presented in for the 5 keV/D case in Fig. 14. The present RE simulation results give not only the total retained D, but quantitative amounts of D trapped in each defect type. Of the total implanted D fluence $5.8\times10^{20}$ D/m$^2$, at 5 keV about 29% is directly backscattered, 63% diffuses to the surface and desorbs to vacuum, and only 8% is retained in the sample.

It was observed that at 5 keV, about 75% of the retained D is trapped in monovacancies and vacancy clusters, and the rest in impurities, grain boundaries and/or dislocations, extending deep into the sample, see Fig. 15. The maximum range for trapped D, increases from about 2.6 $\mu$m at 5 keV, to about 4.5 $\mu$m at 30 keV. These deep extending D tails, have also been observed in other experiments, for example by Alimov *et al.*[219]. At higher fluences,

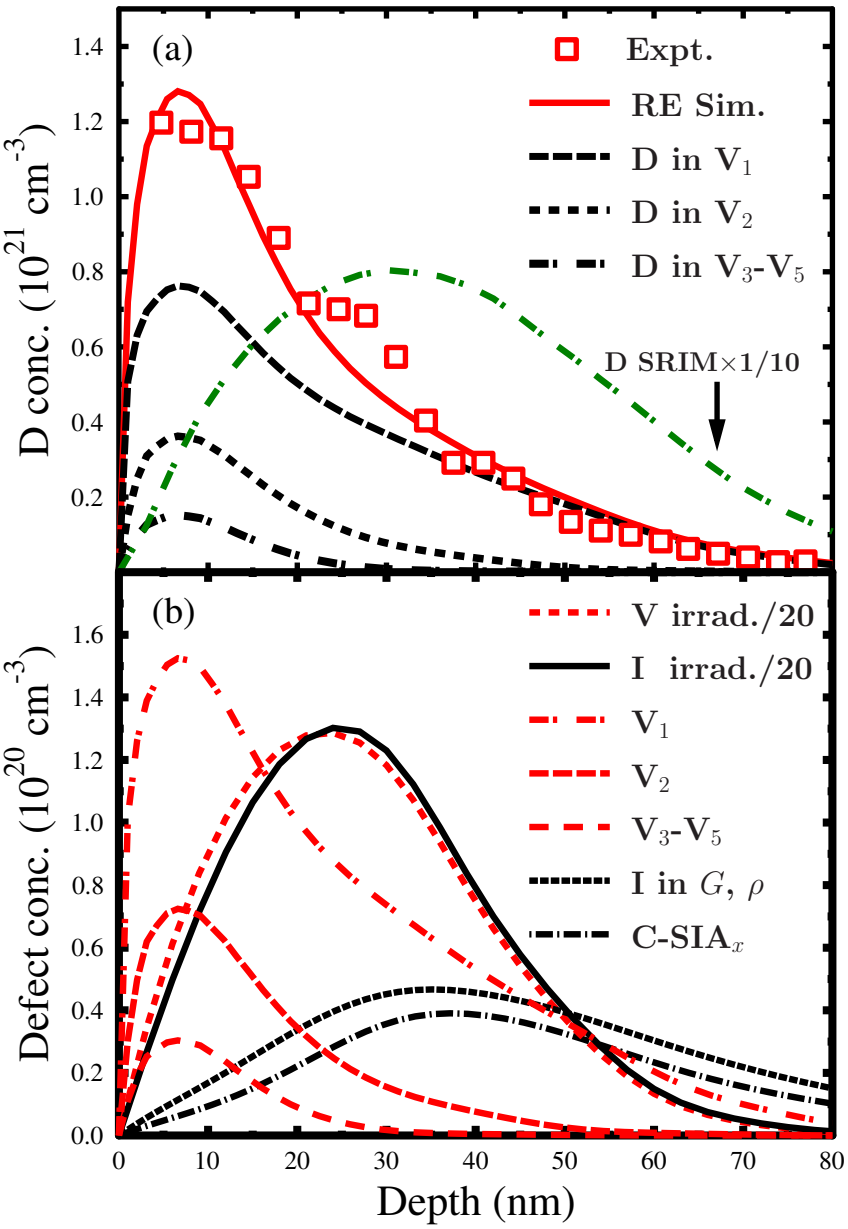


**Figure 14.** Data for the 5 keV/D implantation. (a) The total simulated D profile (solid line) consists mainly of D trapped in monovacancies, while the concentration of D trapped in larger vacancy clusters, decreases along with the cluster size. The SRIM simulation, shows the D profile in case where the implantation would have been done at a temperature where D is immobile (i.e. in the absence of the diffusion that is included in the rate equation (RE) simulations). (b) Implantation induced and final defect profiles. The remaining (about 5 % of the initially produced) self-interstitial atoms (SIAs) in the sample are in grain boundaries ($G$), dislocations ($\rho$) and in carbon impurity $SIA_x$ clusters.

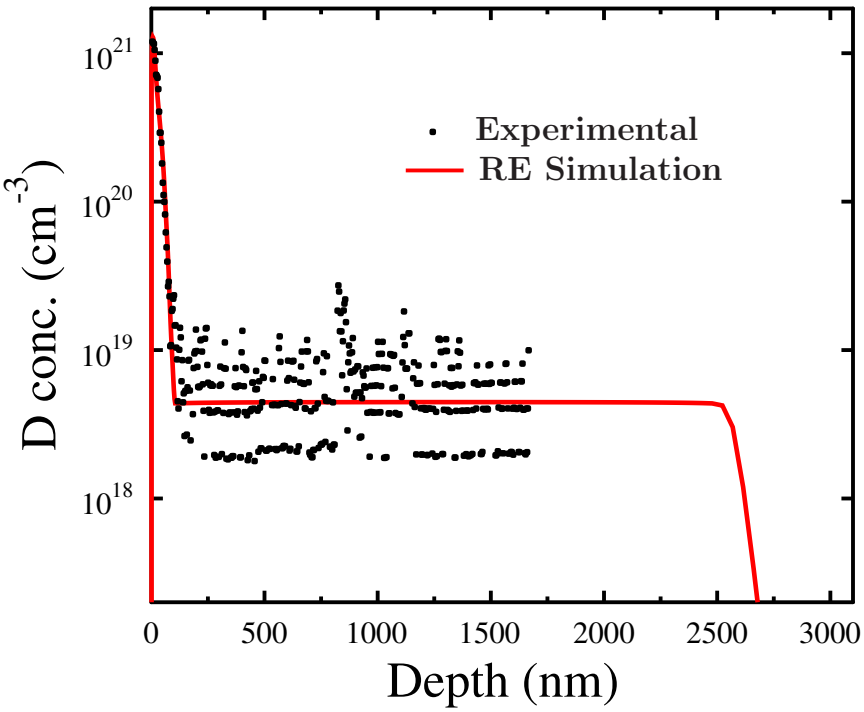


**Figure 15.** The experimental and simulated 5 keV/D profiles in logarithmic scale. The simulation was done by adding a D trapping impurity concentration of $4.5\times10^{15}$ cm$^{-3}$.

the retained fraction deep in the sample, will eventually be much larger than the fraction close to the surface, which will be especially important for tritium retention. The nature of these deep extending traps is not clear, however. They have been observed in both polycrystalline and single crystal material, with the mean trapped D amount being higher in coarse grained, than in single crystal W [219], indicating that part of these D traps could be grain boundaries. The binding of D atoms to grain boundary has been studied by Zhou *et al.* using DFT [220]. Their result suggests a binding energy between 0.8 and 1.5 eV, which certainly would trap D at room temperature.

The present samples are not coarse grained, and the number of trapping sites at grain boundaries, should not alone be sufficient to account for the experimental value of about $5\times10^{24}$/m$^3$. A dislocation density of about $10^{14}$/m$^2$, is also too low to explain the traps. Another additional alternative is, that D is trapped in impurities. One potential trapping impurity present in the sample is oxygen (5 $\mu$g/g). Haasz *et al.* noticed that the D and O depth profiles were quite similar in single crystal W [221]. This finding is a strong indication that O binds D, and DFT calculations are underway to confirm this and to give a value for the binding energy.

Fig. 14(b) shows the irradiation induced and the final defect profiles. The irradiation induced profiles, are the sum self-interstitial atom (SIA) and vacancy profiles times the implanted fluence. The total number of irradiation-induced vacancies and SIAs, per incoming D, is 0.16 at 5 keV, 0.79 at 15 keV, and 1.6 at 30 keV. About 93 - 96% of these vacancies are

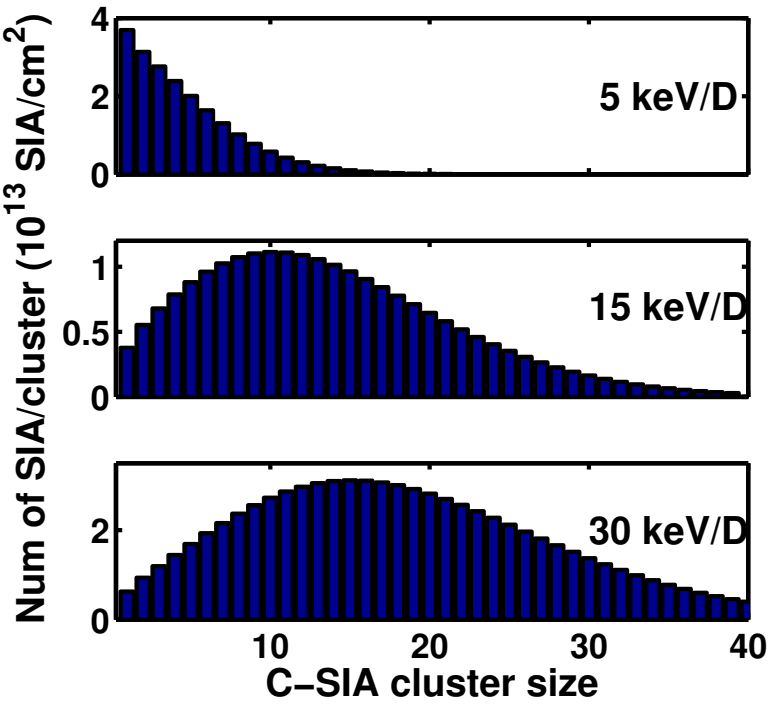


**Figure 16.** Number of different sized C-SIA clusters for increasing implantation energy. The mean number of SIAs per cluster is about 5 for 5 keV, 14 for 15 keV and 18 for 30 keV.

annihilated by the diffusing SIAs during the irradiation. The remaining SIAs in the sample have been trapped by dislocations and grain boundaries and C-SIA$_x$ clusters, where $x$ is the number of SIAs in the cluster. The size distributions of the C-SIA$_x$ clusters are shown in Fig. 16, where the total integrated amount of SIAs in these clusters, increases from about $2.1\times10^{18}$/m$^2$ for 5 keV to about $8.1\times10^{18}$/m$^2$ for 30 keV implantation. Also, the average cluster size is seen to increase, as more SIAs are produced at higher D implantation energies. These C-SIA$_x$ clusters could be the experimentally observed interstitial type dislocation loops [222].

The flux of D, and the corresponding SIA production rate, is too small for producing large SIA or D-SIA clusters. Large SIA clusters were only observed, if it was assumed that there is an impurity that initially forms a bound complex with a SIA. This complex then serves as a nucleation site for large impurity-SIA clusters. If the SIA production rate would be large enough, large SIA clusters could form without the need of impurities. Further evidence for the formation of impurity-SIA complexes, is given by the 8 keV H irradiation experiment by Sakamoto *et al.*[223], showing that the interstitial dislocation loop areal density increases when the impurity concentration increases.

A remarkable observation is that the final retained D profile, Fig. 14(a), does not resemble neither the implanted D, nor the irradiation induced vacancy profile Fig. 14(b). During the D induced collision cascades, the vacancies are produced on average, a bit closer to the surface than the SIAs. The SIA-vacancy annihilation is proportional to both their

respective concentrations, resulting in that vacancies deeper than about 30 nm, are effectively annihilated, and therefore, the remaining vacancy profile is shifted towards the surface. Hence, any short time and D fluence simulation method trying to produce the observed retained D profile will fail, because the vacancy, and in the vacancies trapped D profiles will shift more and more towards the surface with increasing D fluence.

Fig. 17 (a) shows the time evolution of the retained D during, and shortly after the 30 keV/D room temperature implantation. In the figure, three distinct regions are elucidated. In region I, the retained D is the same as the implanted one (100% retention, backscattered fraction excluded).

In region II, the vacancies become saturated with D, and the mean number of trapped D per vacancy, is between five and six. All the implanted D atoms are no longer trapped, but diffuse deeper into the sample, and to the sample surface. In Fig. 17 (b) is shown the simultaneous onset of D atom flux to the W surface. After the implantation has stopped (region III), the D retention drops and a remnant D flux to the W surface takes place for about 10 min. The simulation results show that the slow decrease in the retained D, is the detrapping of the sixth D from monovacancies (trapping energy 0.61 eV). This post implantation effect has been seen experimentally for example by García-Rosales *et al.*[224] and Pisarev *et al.*[225] where the observed $D_2$ desorption from the sample surface, resembles the present simulated D flux to surface in Fig. 17 (b).

### *5.2. He bubble and fuzz formation in W*

Recent experiments [48] have shown that He bombardment of W can lead to the formation of a highly underdense fuzz-like morphology under fusion relevant conditions [226], such as substrate temperatures of $1000-2000$ K [227], low irradiation energies ($\leq 30$ eV) [228] and He fluxes of$10^{20}-10^{23}\mathrm{m}^{-2}\mathrm{s}^{-1}$ [229]. However, the underlying mechanisms remains unclear. Some theoretical models explain the phenomena qualitatively, for instance based on W viscoelasticity [230], stress-driven bubble growth [231] or adatom diffusion [232]. As a step forward, Lasa *et al.* [233] developed a multiscale model where insights from MD simulations on He bubble development The model is based on the balance between the surface growth due to the He bubble formation and consequent dislocation loop punching, and the drop by bubble blistering, leading to a stochastic surface evolution that explains the square root of time dependence and gives quantitative agreement with experiments (see Fig. 18). However, no model has addressed yet key issues such as the upper and lower temperature thresholds for the fuzz formation or the growth rate saturation with increasing the flux.

Further, the general interaction of He with the pre-existing defects in (bulk) W, including the damage caused by energetic $\alpha$ (He) particles, is gaining relevance in the plasma-wall interaction studies. For example, a detailed multiscale model was developed by Becquart *al.*, combining the DFT [235, 236, 237] and KMC [238] methods, to explain the dynamics of He and point defects in W.

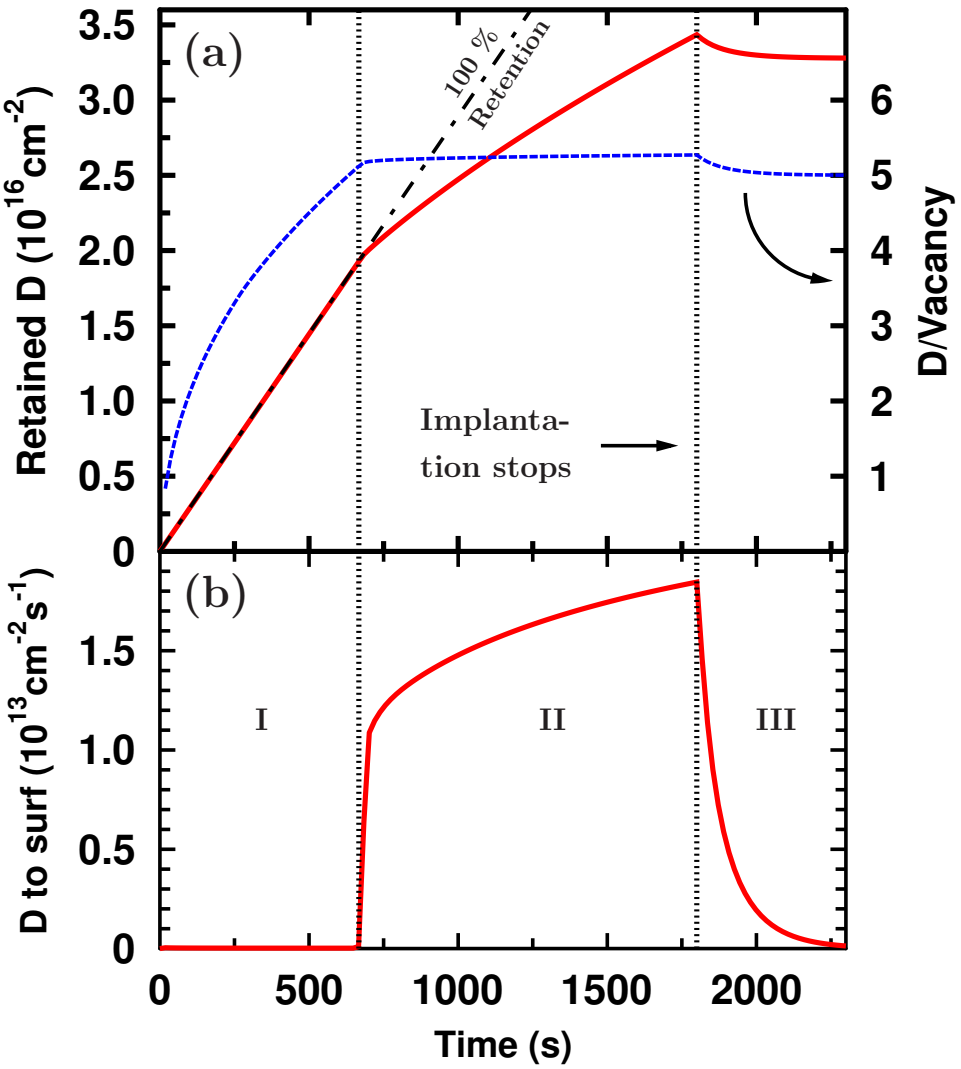


**Figure 17.** (a) Retained D and the mean number of D trapped per vacancy, during and after 30 keV/D room temperature implantation. (b) The flux of D atoms from bulk to sample surface. Region I: Vacancies are slowly filling up with D, 100 % retention. Region II: Vacancies are saturated with D, and D flux to surface starts. Region III: Weakly bound sixth D detraps from vacancies after the implantation.

## 6. Summary

In this Review article, we gave an overview of the physics and chemistry of plasma-wall interactions in tokamak-like fusion reactors, and presented some of the most commonly used materials simulation approaches used to study these. We described the swift chemical sputtering mechanism, and showed how it can explain the erosion of molecular species from both carbon- and beryllium-based first wall materials. We further discussed the atom-level mechanisms of mixed material formation of the reactors, and how binding chemistry affects their sputtering. Finally we showed how rate equations, parametrized from lower-

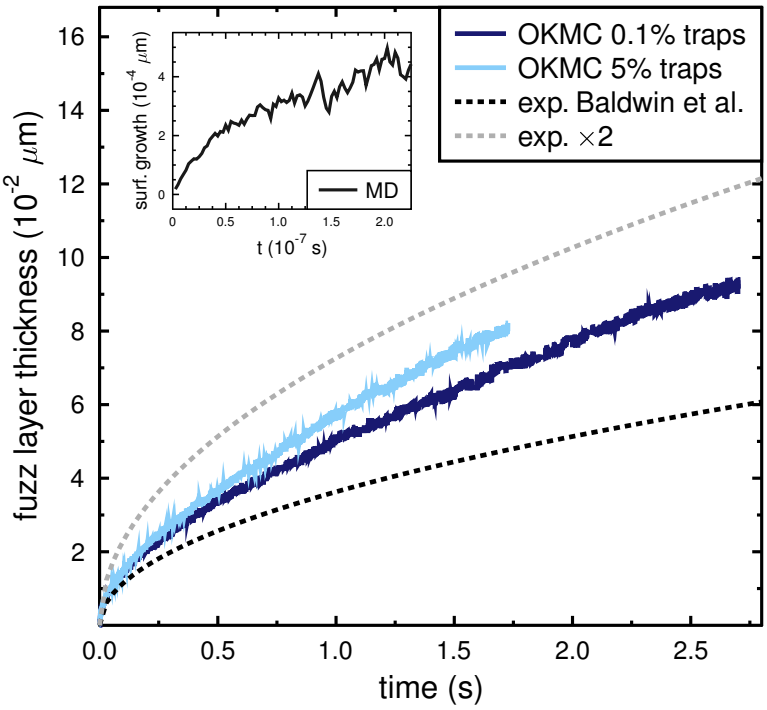


**Figure 18.** The fuzz layer thickness growth as a function of time. The OKMC results (thick lines) were obtained using the parameters taken from [48], for different defect concentrations. The experimental growth rate (*exp*) is interpolated from the results in Ref. [48]. The upper boundary *exp.2* is calculated as double that of *exp*, accounting for factors such as the W-grade [234]. The surface growth in MD [195] is shown for a comparison, plotted separately as the time scales differ by 7 orders of magnitude.

level simulation methods in a multiscale scheme can be used to describe the hydrogen isotope diffusion and retention in tungsten-based fusion reactor divertors.

## Acknowledgements

This work, supported by the European Communities under the contract of Association between EURATOM/Tekes, was carried out within the framework of the European Fusion Development Agreement. Partial support was also received from the EURATOM 7th framework programme, under grant agreement number 212175 (GetMat project). The views and opinions expressed herein do not necessarily reflect those of the European Commission. Grants of computer time from the Centre for Scientific Computing in Espoo, Finland, are gratefully acknowledged. We also are grateful to Mr. Arrak Punsch for continuous inspiration during the course of the work.

## References


[1] J. Wesson. *Tokamaks*. Number 48 in Oxford Engineering Series. Clarendon Press, Oxford, 2nd edition, 1997.

[2] ITER Physics Basis Editors, ITER Physics Expert Group Chairs and Co-Chairs and ITER Joint Central Team and Physics Integration Unit. Iter physics basis. *Nuclear Fusion*, 39:2137–2638, 1999.

[3] Wan Baonian. Physical engineering test and first divertor plasma configuration in east. *Plasma Science and Technology*, 9(2):125, 2007.

[4] T. Kurki-Suonio, V. Hynönen, T. Ahlgren, K. Nordlund, K. Sugiyama, R. Dux, and the ASDEX Upgrade Team4. Fusion tritons and plasma-facing components in a fusion reactor. *Europhys. Lett.*, 78:65002, 2007.

[5] M. Victoria, S. Dudarev, J. L. Boutard, E. Diegele, R. Lässer, A. Almazouzi, M. J. Caturla, C. C. Fu, J. Källne, L. Malerba, K. Nordlund, M. Perlado, M. Rieth, M. Samaras, R. Schaeublin, B. Singh, and F. Willaime. Modeling irradiation effects in fusion materials. *Fusion and engineering design*, 82:2413–2421, 2007.

[6] S.L. Dudarev, J.-L. Boutard, R. Lässer, M.J. Caturla, P.M.Derlet, M. Fivel, C.-C. Fu, M.Y. Lavrentiev, L. Malerba, M. Mrovec, D. Nguyen-Manh, K. Nordlund, M. Perlado, R. Schäublin, H. Van Swygenhoven, D. Terentyev, J. Wallenius, D. Weygand, and F. Willaime. The eu programme for modelling radiation effects in fusion reactor materials: An overview of recent advances and future goals. *J. Nucl. Mater.*, 386-388:1–7, 2009.

[7] W. R. Grove. On the electro-chemical polarity of gases. *Phil. trans. Roy. Soc. London*, 142:87, 1852.

[8] N. Bohr. On the theory of the decrease of velocity of moving electrified particles on passing through matter. *Phil. Mag.*, 25:10–, 1913.

[9] E. Rutherford. The scattering of $\alpha$ and $\beta$ rays by matter and the structure of the atom. *Phil. Mag.*, 6:31, 1911.

[10] J. A. Leavitt, L. C. McIntyre, Jr., and M. R. Weller. *Backscattering spectrometry*. Materials Reseach Society, Pittsburgh, Pennsylvania, 1995.

[11] Leonard C. Feldman and James W. Mayer. *Fundamentals of Surface and Thin Film Analysis*. North-Holland, New York, 1986.

[12] Robert F. Hochman, editor. *Ion plating and implantation. Applications to materials*, Materials Park, Ohio, 1986. American Society for Metals.

[13] J. M. E. Harper, J. J. Cuomo, and H. T. G. Hentzell. Synthesis of compound thin films by dual ion beam deposition. i. experimental approach. *J. Appl. Phys.*, 58(1):550–55, 1985.

[14] W. L. Brown, M. F. Jarrold, R. L. McEachern, M. Sosnowski, H. Usui G. Takaoka, and I. Yamada. Ion cluster beam deposition of thin films. *Nucl. Instr. Meth. Phys. Res. B*, 59-60:182–189, 1991.

[15] James W. Mayer and S. S. Lau. *Electronic Materials Science For Integrated Circuits in Si and GaAs*. MacMillan, New York, 1990.

[16] M. Nastasi, J. Mayer, and J. Hirvonen. *Ion-Solid Interactions - Fundamentals and Applications*. Cambridge University Press, Cambridge, Great Britain, 1996.

[17] A. V. Krasheninnikov and K. Nordlund. Ion and electron irradiation-induced effects in nanostructured materials. *J. Appl. Phys. (Applied Physics Reviews)*, 107:071301, 2010.

[18] M. Merola, public presentation at the 16th International Conference on Fusion Reactor Materials, Oct 21, 2013, Beijing, China.

[19] J. A. Brinkman. On the nature of radiation damage in metals. *J. Appl. Phys.*, 25:961, 1954.

[20] T. Diaz de la Rubia, R. S. Averback, R. Benedek, and W. E. King. Role of thermal spikes in energetic collision cascades. *Phys. Rev. Lett.*, 59:1930–1933, 1987. See also erratum: Phys. Rev. Lett. 60 (1988) 76.

[21] R. S. Averback and T. Diaz de la Rubia. Displacement damage in irradiated metals and semiconductors. In H. Ehrenfest and F. Spaepen, editors, *Solid State Physics*, volume 51, pages 281–402. Academic Press, New York, 1998.

[22] T. Diaz de la Rubia and M. W. Guinan. New mechanism of defect production in metals: A molecular-

dynamics study of interstitial-dislocation-loop formation at high-energy displacement cascades. *Phys. Rev. Lett.*, 66:2766, 1991.

[23] M. Ghaly, K. Nordlund, and R. S. Averback. Molecular dynamics investigations of surface damage produced by kev self-bombardment of solids. *Phil. Mag. A*, 79(4):795, 1999.

[24] K. Nordlund, J. Tarus, J. Keinonen, S. E. Donnelly, and R. C. Birtcher. Atomic fingers, bridges and slingshots: formation of exotic surface structures during ion irradiation of heavy metals. *Nucl. Instr. Meth. Phys. Res. B*, 206:189–193, 2003.

[25] R. Behrisch (ed.). *Sputtering by Particle bombardment I*. Springer, Berlin, 1981.

[26] Peter Sigmund. Introduction to sputtering. *Matematisk Fysiske Meddelelser Kongelige Danske Videnskabernes Selskab*, 43:7–26, 1993.

[27] K. L. Merkle and W. Jäger. Direct observation of spike effects in heavy-ion sputtering. *Phil. Mag. A*, 44:741, 1981.

[28] Mai Ghaly and R. S. Averback. Effect of viscous flow on ion damage near solid surfaces. *Phys. Rev. Lett.*, 72(3):364–367, 1994.

[29] P. D. Townsend. Ion implantation – an introduction. *Contemp. Phys.*, 27(3):241, 1986.

[30] M. A. Kirk, I. M. Robertson, M. L. Jenkins, C. A. English, T. J. Black, and J. S. Vetrano. The collapse of defect cascades to dislocation loops. *J. Nucl. Mater.*, 149:21, 1987.

[31] S. J. Zinkle. Fundamental radiation effects parameters in metals and ceramics. *Rad. Eff. & Def. in Sol.*, 148:447–477, 1999.

[32] M. Kiritani, T. Yoshiie, and S. Kojima. Factors controlling the nature and amount of residual defects in neutron irradiated metals. *J. Nucl. Mater.*, 141-143:625–632, 1986.

[33] S. Kojima, Y. Satoh, H. Taoka, I. Ishida, T. Yoshie, and M. Kiritani. Confirmation of vacancy-type stacking fault tetrahedra in quenched, deformed and irradiated face-centred cubic metals. *Phil. Mag. A*, 59(3):519–532, 1989.

[34] K. Nordlund and F. Gao. Formation of stacking fault tetrahedra in collision cascades. *Appl. Phys. Lett.*, 74(18):2720–2722, 1999.

[35] M. O. Ruault, J. Chaumont, J. M. Penisson, and A. Bourret. High resolution and in situ investigation of defects in bi-irradiated si. *Phil. Mag. A*, 50(5):667, 1984.

[36] T. Diaz de la Rubia and G. H. Gilmer. Structural transformations and defect production in ion implanted silicon: A molecular dynamics simulation study. *Phys. Rev. Lett.*, 74(13):2507–2510, 1995.

[37] S. A. Norris, J. Samela, C. S. Madi, M. P. Brenner, L. Bukonte, M. Backman, F. Djurabekova, K. Nordlund, and M. J. Aziz. Md-predicted phase diagrams for pattern formation. *Nature communications*, 2:276, 2011.

[38] S. Dhara. Formation, dynamics, and characterization of nanostructures by ion beam irradiation. *Critical Reviews in Solid State and Materials Sciences*, 32:1–50, 2007.

[39] R. Salh, L. Fitting, E. V. Kolesnikova, A. A. Sitnikova, M. V. Zamoryanskaya, B. Schmidt, and H. J. Fitting. Si and ge nanocluster formation in silica matrix. *Semiconductors*, 41(4):381, 2007.

[40] S. E. Donnelly, R. C. Birtcher, C. Templier, and V. Vishnyakov. Response of helium bubbles in gold to displacement-cascade damage. *Phys. Rev. B*, 52(6):3970, 1995.

[41] R. C. Birtcher, S. E. Donnelly, M. Song, K. Furuya, K. Mitsuishi, and C. W. Allen. Behavior of crystalline xe nanoprecipitates during coalescence. *Phys. Rev. Lett.*, 83(8):1617, 1999.

[42] J. B. Condon and T. Schober. Hydrogen bubbles in metals. *J. Nucl. Mater.*, 207:1–24, 1993.

[43] J. W. Mayer. Ion implantation-lattice disorder. In J. W. Corbett and G. D. Watkins, editors, *Radiation Effects in Semiconductors*, page 367. Gordon & Breach, 1971.

[44] K. Nordlund, J. Keinonen, E. Rauhala, and T. Ahlgren. Range profile in self-ion-implanted crystalline si. *Phys. Rev. B*, 52:15170, 1995.

[45] E. Chason, S. T. Picraux, M. Poate, J. O. Borland, M. I. Current, T. Diaz de la Rubia, D. J. Eaglesham, O. W. Holland, M. E. Law, C. W. Magee, J. W. Mayer, J. Melngailis, and A. F. Tasch. Ion beams in silicon processing and characterization. *J. Appl. Phys*, 81(10):6513–6561, 1997.

[46] Lourdes Pelaz, Luis A. Marqués, Maria Aboy, Juan Barbolla, and George H. Gilmer. Atomistic modeling of amorphization and recrystallization in silicon. *Appl. Phys. Lett.*, 82(13):2038, 2003.

[47] B. Stritzker, R. G. Elliman, and J. Zou. Self-ion-induced swelling of germanium. *Nucl. Instr. Meth. Phys. Res. B*, 175:193, 2000.

[48] M. J. Baldwin and R. P. Doerner. Helium induced nanoscopic morphology on tungsten under fusion relevant plasma conditions. *Nuclear Fusion*, 48:035001, 2008.

[49] Shin Kajita, Naoaki Yoshida, Reiko Yoshihara, Noriyasu Ohno, and Masato Yamagiwa. Tem observation of the growth process of helium nanobubbles on tungsten: Nanostructure formation mechanism. *J. Nucl. Mater.*, 418:152–158, 2011.

[50] A. Loarte. Implications of the use of carbon-based plasma facing components in next step fusion devices. *Physica Scripta*, T111:13–22, 2004.

[51] W. Wang, J. Roth, S. Lindig, and C. H. Wu. Blister formation of tungsten due to ion bombardment. *J. Nucl. Mater.*, 299:124, 2001.

[52] M. Nishikawa. High flux dependence of erosion and retention in beam experiments and its significance to fusion systems. *Fusion Engineering and Design*, 41:47–53, 1998.

[53] B. Lipschultz, J. Roth, J. W. Davis, R. P. Doerner, A. A. Haasz, A. Kalenbach, A. Kirschner, R. D. Kolasinski, A. Loarte, V. Philipps, K. Schmid, W. R. Wampler, G. M. Wright, and D. G. Whyte. An assessment of the current data affecting tritium retention and its use to project towards t retention in iter. Technical Report PSFC/RR-10-4, MIT, 2010.

[54] J. Küppers. The hydrogen surface chemistry of carbon as a plasma facing material. *Surf. Sci. Rep.*, 22:249–321, 1995.

[55] M. T. Robinson and Ian M. Torrens. Computer simulation of atomic-displacement cascades in solids in the binary-collision approximation. *Phys. Rev. B*, 9(12):5008, 1974.

[56] E. Snoeks, A. Polman, and C. A. Volkert. Densification, anisotropic deformation, and plastic flow of $sio_2$ during mev heavy ion irradiation. *Appl. Phys. Lett.*, 65(19):2487, 1994.

[57] R. O. Jones and O. Gunnarsson. *Rev. Mod. Phys.*, 61:689, 1989.

[58] For a review, see R. O. Jones and O. Gunnarsson, Rev. Mod. Phys. **61**, 689 (1989).

[59] S. Uhlmann, Th. Frauenheim, K. J. Boyd, D. Marton, and J. W. Rabalais. Elementary processes during low-energy self-bombardment of si(100) $2 \times 2$ - a molecular dynamics study. *Rad. Eff. & Def. in Sol.*, 141:185, 1997.

[60] A. V. Krasheninnikov, K. Nordlund, E. Salonen, J. Keinonen, and C. H. Wu. Sputtering of amorphous hydrogenated carbon by hyperthermal ions as studied by tight-binding molecular dynamics. *Comput. Mater. Sci*, 25:427–434, 2002.

[61] E. Holmström, A. Kuronen, and K. Nordlund. Threshold defect production in silicon determined by density functional theory molecular dynamics simulations. *Phys. Rev. B*, 78(4):045202, 2008.

[62] T. Korhonen, M. J. Puska, and R. M. Nieminen. Vacancy formation energies for fcc and bcc transition metals. *Phys. Rev. B*, 51(15):9526, 1996.

[63] Karin Carling, Göran Wahnström, Thomas R. Mattsson, Nils Sandberg, and Göran Grimvall. Vacancy concentration in al from combined first-principles and model potential calculations. *Phys. Rev. B*, 67:054101, 2003.

[64] Chu-Chun Fu, F. Willaime, and P. Ordejon. Stability and mobility of mono- and di-interstitials in $\alpha$-fe. *Phys. Rev. Lett.*, 92(17):175503–1, 2004.

[65] P. A. Korzhavyi, A. V. Ruban, A. Y. Lozovoi, Yu. Kh. Vekilov, I. A. Abrikosov, and B. Johansson. Constitutional and thermal point defects in b2 nial. *Phys. Rev. B*, 61(9):6003, 2000.

[66] Y. Mishin, A. Y. Lozovoi, and A. Alavi. Evaluation of diffusion mechanisms in nial by embedded-atom and first-principles calculations. *Phys. Rev. B*, 67:014201, 2003.

[67] P. Olsson, I.A. Abrikosov, L. Vitos, and J. Wallenius. Ab initio formation energies of fe-cr alloys. *J. Nucl.. Mater*, 321:84, 2003.

[68] M. J. Puska, S. Pöykkö, M. Pesola, and R. M. Nieminen. Convergence of supercell calculations for point defects in semiconductors: vacancy in silicon. *Phys. Rev. B*, 58:1318–1325, 1998.

[69] T. Mattila and R. M. Nieminen. Direct antisite formation in electron irradiation of gaas. *Phys. Rev. Lett.*, 74:2721, 1995.

[70] P. Erhart, K. Albe, and A. Klein. First-principles study of intrinsic point defects in zno: Role of band

structure, volume relaxation and finite size effects. *Phys. Rev. B*, 2006.

[71] Anderson Janotti and Chris G. Van de Walle. Native point defects in ZnO. *Phys. Rev. B*, 76(16), 2007.

[72] F. Gupta, G. Brillant, and A. Pasturel. Correlation effects and energetics of point defects in uranium dioxide: a first principle investigation. *Phil. Mag.*, 87(16-17):2561–2569, 2007.

[73] M. T. Robinson and O. S. Oen. The channeling of energetic atoms in crystal lattices. *Appl. Phys. Lett.*, 2(4):30, 1963.

[74] R. Smith (ed.). *Atomic & ion collisions in solids and at surfaces: theory, simulation and applications*. Cambridge University Prss, Cambridge, UK, 1997.

[75] J. F. Ziegler, J. P. Biersack, and U. Littmark. *The Stopping and Range of Ions in Matter*. Pergamon, New York, 1985.

[76] J. F. Ziegler. SRIM-2013 software package, available online at *http://www.srim.org*.

[77] J. F. Ziegler, J. P. Biersack, and M. D. Ziegler. *SRIM - The Stopping and Range of Ions in Matter*. SRIM Co., Chester, Maryland, USA, 2008.

[78] W. Möller and W. Eckstein. Tridyn - a trim simulation code including dynamic composition changes. *Nucl. Instr. Meth. Phys. Res. B*, 2:814, 1984.

[79] T. S. Pugacheva, F. G. Djurabekova, and S. Kh. Valiev. Effects of cascade mixing, sputtering and diffusion by high dose light ion irradiation of boron nitride. *Nucl. Instr. Meth. Phys. Res. B*, 141:99–104, 1998.

[80] Mark T. Robinson. Computer simulation studies of high-energy collision cascades. *Nucl. Instr. Meth. Phys. Res. B*, 67:396, 1992.

[81] M. Posselt and J. P. Biersack. Computer-simulation of ion-implantation into crystalline targets. *Nucl. Instr. Meth. Phys. Res. B*, 64:706, 1992.

[82] R.E. Stoller, M. B. Toloczko, G. S. Was, A. G. Certain, S. Dwaraknath, and F.A. Garner. On the use of srim for computing radiation damage exposure. *Nucl. Instr. Meth. Phys. Res. B*, 310:75, 2013.

[83] J. Likonen and M. Hautala. Binary collision lattice simulation study of model parameters in monocrystalline sputtering. *J. Phys.: Condens. Matter*, 1:4697, 1989.

[84] K. O. E. Henriksson, K. Vörtler, S. Dreißigacker, K. Nordlund, and J. Keinonen. Sticking of atomic hydrogen on the tungsten (001) surface. *Surf. Sci.*, 600:3167–3174, 2006.

[85] W. Möller. A computer study of the collisional mixing of pt in si. *Nucl. Instr. Meth. Phys. Res. B*, 15:688, 1986.

[86] M. Mayer and W. Eckstein. Monte carlo calculations of hydrogen and deuterium range distributions in light target materials. *Nucl. Instr. Meth. Phys. Res. B*, 94:22, 1994.

[87] R. G. Vichev and D. S. Karpuzov. Time evolution of ion slowing-down in amorphous solids. *Nucl. Instr. Meth. Phys. Res. B*, 83:345, 1993.

[88] K. Gärtner *et. al.* Round robin compbuter simulation of ion transmission through crystalline layers. *Nucl. Instr. Meth. Phys. Res. B*, 102(1-4):183, 1995.

[89] G. Hobler and D. Kovac. Dynamic binary collision simulation of focused ion beam milling of deep trenches. *Nucl. Instr. Meth. Phys. Res. B*, 269(14):1609, 2011.

[90] L. Bukonte, F. Djurabekova, J. Samela, K. Nordlund, S. A. Norris, and M. J. Aziz. Comparison of molecular dynamics and binary collision approximation simulations for atom displacement analysis. *Nucl. Instr. Meth. Phys. Res. B*, 297:23–28, 2013.

[91] A. Lasa, K. Schmid, and K. Nordlund. Modelling of w-be mixed material sputtering under h irradiation. *Physica Scripta*, T159:014059, 2014.

[92] A. Kirschner, V. Philipps, J. Winter, and U. Kögler. Simulation of the plasma-wall interaction in a tokamak with the monte carlo code ERO-TEXTOR. *Nuclear Fusion*, 40:989, 2000.

[93] H. Plank, W. Wang, W. Eckstein, R. Schwörer, H. J. Steffen, and J. Roth. Deposition and hydrogen content of carbon films grown by $ch_3^+$ ion-beam bombardment. *J. Appl. Phys.*, 78(9):5366, 1995.

[94] H. Plank and W. Eckstein. Preferential sputtering of carbides under deuterium irradiation - a comparison between experiment and computer simulation. *Nucl. Instr. Meth. Phys. Res. B*, 124:23–30, 1997.

[95] W. Eckstein, R. Dohmen, A. Mutzke, and R. Schneider. SDTrimSP: A Monte-Carlo Code for Calculating Collision Phenomena in Randomized Targets, *http://edoc.mpg.de/287291*.

[96] M. P. Allen and D. J. Tildesley. *Computer Simulation of Liquids*. Oxford University Press, Oxford,

England, 1989.

[97] R. Lesar. *Introduction to Computational Materials Science*. Cambridge University Press, 2013.

[98] Andrew R. Leach. *Molecular modelling: principles and applications*. Pearson Education, Harlow, England, 2nd edition, 2001.

[99] Daan Frenkel and Berend Smit. *Understanding molecular simulation: from algoritms to applications*. Academic Press, San Diego, second edition, 2002.

[100] K. Nordlund. Molecular dynamics simulation of ion ranges in the 1 – 100 kev energy range. *Comput. Mater. Sci.*, 3:448, 1995.

[101] K. Nordlund, M. Ghaly, R. S. Averback, M. Caturla, T. Diaz de la Rubia, and J. Tarus. Defect production in collision cascades in elemental semiconductors and fcc metals. *Phys. Rev. B*, 57(13):7556–7570, 1998.

[102] E. Zarkadoula, M. T. Dove, K. Trachenko, S. L. Daraszewicz, D. M. Duffy, , M. Seaton, I. T. Todorov, and K. Nordlund. The nature of high-energy radiation damage in iron. *J. Phys. Condens. Matt.*, 25(12):125402, 2013.

[103] Donald W. Brenner. Empirical potential for hydrocarbons for use in simulating the chemical vapor deposition of diamond films. *Phys. Rev. B*, 42(15):9458, 1990. ; *idem*, 46, 1948 (1992).

[104] D. W. Brenner, O. A. Shenderova, J. A. Harrison, S. J. Stuart, and S. B. Sinnott. A second-generation reactive empirical bond order (rebo) potential energy expression for hydrocarbons. *J. Phys.: Condens. Matter*, 14:783–802, 2002.

[105] S. J. Stuart, A. B. Tutein, and J. A. Harrison. A reactive potential for hydrocarbons with intermolecular interactions. *J. Chem. Phys.*, 112:6472, 2000.

[106] Adri C. T. van Duin, Siddharth Dasgupta, Francois Lorant, and William A. Goddard III. Reaxff: A reactive force field for hydrocarbons. *J. Phys. Chem. A*, 105:9396, 2001.

[107] E. Salonen, K. Nordlund, J. Tarus, T. Ahlgren, J. Keinonen, and C. H. Wu. Suppression of carbon erosion by hydrogen shielding during high-flux hydrogen bombardment. *Phys. Rev. B (Rapid Comm.)*, 60:14005, 1999.

[108] E. Salonen, K. Nordlund, J. Keinonen, and C. H. Wu. Bond-breaking mechanism of sputtering. *Europhysics Letters*, 52(5):504–510, 2000.

[109] E. Salonen, K. Nordlund, J. Keinonen, and C. H. Wu. Swift chemical sputtering of amorphous hydrogenated carbon. *Phys. Rev. B*, 63:195415, 2001.

[110] E. Salonen. Overview of the atomistic modeling of the chemical erosion of carbon. *Physica Scripta*, T111:133–137, 2004.

[111] D. A. Alman and D. N. Ruzic. Molecular dynamics calculation of carbon/hydrocarbon reflection coefficients on a hydrogenated graphite surface. *J. Nuclear Materials*, 313-316:182–6, 2003.

[112] J. Marian, L. A. Zepeda-Ruiz, N. Couto, E. M. Bringa, G. H. Gilmer, P. C. Stangeby, and T. D. Rognlien. X. *J. Appl. Phys.*, 101:044506, 2007.

[113] P. S. Krstic, C. O. Reinhold, and S. Stuart. Chemical sputtering from amorphous carbon under bombardment by deuterium atoms and molecules. *New J. Phys.*, 9:209, 2007.

[114] P. S. Krstic, C. O. Reinhold, and S. Stuart. Chemical sputtering by impact of excited molecules. *EPL*, 77(33002), 2007.

[115] P. N. Maya, U. von Toussaint, and C. Hopf. Synergistic erosion process of hydrocarbon films: A molecular dynamics study. *New J. Phys.*, 10:023002, 2008.

[116] M. W. Finnis and J. E. Sinclair. A simple empirical n-body potential for transition metals. *Phil. Mag. A*, 50(1):45, 1984. *see also Erratum, ibid. 53 (1986) 161*.

[117] Murray S. Daw, Stephen M. Foiles, and Micael I. Baskes. The embedded-atom method: a review of theory and applications. *Mat. Sci. Rep.*, 9:251, 1993.

[118] C. L. Kelchner, D. M. Halstead, L. S. Perkins, N. M. Wallace, and A. E. DePristo. Construction and evaluation of embedding functions. *Surf. Sci.*, 310:425–435, 1994. and references therein.

[119] F. Cleri and V. Rosato. Tight-binding potentials for transition metals and alloys. *Phys. Rev. B*, 48(1):22, 1993.

[120] S. L. Dudarev and P. M. Derlet. A magnetic interatomic potential for molecular dynamics simulations. *J.*

*Phys.: Condens. Matter*, 17:1–22, 2005.

[121] J. Tersoff. New empirical approach for the structure and energy of covalent systems. *Phys. Rev. B*, 37:6991, 1988.

[122] K. Albe, K. Nordlund, J. Nord, and A. Kuronen. Modelling of compound semiconductors: Analytical bond-order potential for ga, as and gaas. *Phys. Rev. B*, 66:035205, 2002.

[123] K. Albe, K. Nordlund, and R. S. Averback. Modeling metal-semiconductor interaction: Analytical bond-order potential for platinum-carbon. *Phys. Rev. B*, 65:195124, 2002.

[124] Paul Erhart, Niklas Juslin, Oliver Goy, Kai Nordlund, Ralf Muller, and Karsten Albe. Analytic bond-order potential for atomistic simulations of zinc oxide. *J. Phys.: Condens. Matter*, 18:6585–6605, 2006.

[125] J. Nord, K. Albe, P. Erhart, and K. Nordlund. Modelling of compound semiconductors: Analytical bond-order potential for gallium, nitrogen and gallium nitride. *Journal of Physics: Condensed Matter*, 15(32):5649–5662, 2003.

[126] N. Juslin, P. Erhart, P. Träskelin, J. Nord, K. O. E. Henriksson, K. Nordlund, E. Salonen, and K. Albe. Analytical interatomic potential for modelling non-equilibrium processes in the w-c-h system. *J. Appl. Phys.*, 98:123520, 2005.

[127] K. O. E. Henriksson and K. Nordlund. Simulations of cementite: An analytical potential for the fe-c system. *Phys. Rev. B*, 79:144107, 2009.

[128] C. Björkas, N. Juslin, H. Timkó, K. Vörtler, K Nordlund, K. O. E. Henriksson, and P Erhart. Interatomic potentials for the beryllium be-c-h system. *J. Phys.: Condens. Matter*, 21(44):445002, 2009.

[129] C. Björkas, K. O. E. Henriksson, M. Probst, and K. Nordlund. A be-w interatomic potential. *J. Phys.: Condens. Matter (fast track communication)*, 22:352206, 2010.

[130] T. Ahlgren, K. Heinola, N. Juslin, and A. Kuronen. Bond-order potential for point and extended defect simulations in tungsten. *J. Appl. Phys.*, 107(3):033516, 2010.

[131] X.-C. Li, X. Shu, Y.-N. Liu, F. Gao, and G.-H. Lu. Modified analytical interatomic potential for a w-h system with defects. *J. Nucl. Mater.*, 408:12–17, 2011.

[132] A. F. Voter and M. R. Sorensen. Accelerating atomistic simulations of defect dynamics: hyperdynamics, parallell replica dynamics, and temperature-accelerated dynamics. In V. V. Bulatov, T. Diaz de la Rubia, R. Phillips, E. Kaxiras, and N. Ghoniem, editors, *Multiscale Modelling of Materials*, volume 538 of *MRS Symp. Proc.*, page 427. Materials Research Society, Pittsburgh, 1999.

[133] A. F. Voter, F. Montalenti, and T. C. Germann. Extending the time scale in atomistic simulation of materials. *Annu. Rev. Mater. Res.*, 32:321–346, 2002.

[134] S. Blackwell, R. Smith, S. D. Kenny, and J. M. Walls. Modeling evaporation, ion-beam assist, and magnetron sputtering of thin metal films over realistic time scales. *Phys. Rev. B*, 86:035416, 2012.

[135] W. M. Young and E. W. Elcock. Monte carlo studies of vacancy migration in binary ordered alloys: I. *Proc. Phys. Soc*, 89:735–746, 1966.

[136] A. B. Bortz, M. H. Kalos, and J. L. Lebowitz. A new algorithm for monte carlo simulation of ising spin systems. *J. Computational Physics*, 17:10–18, 1975.

[137] K. A. Fichthorn and W. H. Weinberg. Theoretical foundations of dynamical monte carlo simulations. *J. Chem. Phys*, 95(2):1090, 1991.

[138] J. Kotakoski, A. V. Krasheninnikov, and K. Nordlund. Kinetic monte carlo simulations of the response of carbon nanotubes to electron irradiation. *J. Computat. and Theor. Nanoscience*, 4:1153–1159, 2007.

[139] F. G. Djurabekova, L. Malerba, C. Domain, and C. S. Becquart. Stability and mobility of small vacancy and copper-vacancy clusters in bcc-fe: An atomistic kinetic monte carlo study. *Nucl. Instr. Meth. Phys. Res. B*, 255(1):47–51, 2007.

[140] L. Pelaz, L. A. Marqués, and J. Barbolla. Ion-beam-induced amorphization and recrystallization in silicon. *J. Applied Physics*, 96(11):5947–5976, 2004.

[141] C. S. Becquart, C. Domain, U. Sarkar, A. DeBacker, and M. Hou. Microstructural evolution of irradiated tungsten: Ab initio parameterisation of an OKMC model. . *Nucl. Mater.*, 403(1-3):75–88, 2010.

[142] J. Dalla Torre, J. Bocquet, N. V. Doan, E. Adam, and A. Barbu. Jerk, an event-based kinetic monte carlo model to predict microstructure evolution of materials under irradiation. *Phil. Mag. A*, 85:549, 2005.

[143] T. Opplestrup, V. V. Bulatov, G. H. Gilmer, M. H. Kalos, and B. Sadigh. First-passage monte carlo

algorithm: Diffusion without all the hops. *Phys. Rev. Lett.*, 97:230602, 2006.

[144] Manoj Warrier, Ralf Schneider, Emppu Salonen, and Kai Nordlund. Multi scale modeling of hydrogen isotope diffusion in graphite. *Contrib. Plasma Phys.*, 44(1-3):307–310, 2004.

[145] R. Schneider, A. Rai, A. Mutzke, M. Warrier, E. Salonen, and K. Nordlund. Dynamic monte-carlo modeling of hydrogen isotope reactive-diffusive transport in porous graphite. *J. Nucl. Mater.*, 367:1238–1242, 2007.

[146] M. Warrier, R. Schneider, E. Salonen, and K. Nordlund. Effect of the porous structure of graphite on atomic hydrogen diffusion and inventory. *Nuclear Fusion*, 47:1656–1663, 2007.

[147] K. O. E. Henriksson, K. Nordlund, A. Krasheninnikov, and J. Keinonen. The depths of hydrogen and helium bubbles in tungsten - a comparison. *Fusion Science & Technology*, 50:43–57, 2006.

[148] M. Rieth, S.L. Dudarev, S.M. Gonzalez de Vicente, J. Aktaa, T. Ahlgren, S. Antusch, D.E.J. Armstrong, M. Balden, N. Baluc, M.-F. Barthe, W.W. Basuki, M. Battabyal, C.S. Becquart, D. Blagoeva, H. Boldyryeva, J. Brinkmann, M. Celino, L. Ciupinski, J.B. Correia, A. De Backer, C. Domain, E. Gaganidze, C. Garciya-Rosales, J. Gibson, M.R. Gilbert, S. Giusepponi, B. Gludovatz, H. Greuner, K. Heinola, T. Höschen, A. Hoffmann, N. Holstein, F. Koch, W. Krauss, H. Li, S. Lindig, J. Linke, Ch. Linsmeier, P. López-Ruiz, H. Maier, J. Matejicek, T.P. Mishra, M. Muhammed, A. Munoz, M. Muzyk, K. Nordlund, D. Nguyen-Manh, J. Opschoor, N. Ordás, T. Palacios, G. Pintsuk, R. Pippan, J. Reiser, J. Riesch, S.G. Roberts, L. Romaner, M. Rosinski, M. Sanchez, W. Schulmeyer, H. Traxler, A. Urena, J.G. van der Laan, L. Veleva, S. Wahlberg yand M. Walter, T. Weber, T. Weitkamp, S. Wurster, M.A. Yar, J.H. You, and A. Zivelonghi. Recent progress in research on tungsten materials for nuclear fusion applications in europe. *J. Nucl. Mater.*, 432(1-3):482–500, 2013.

[149] D. Hull and D. J. Bacon. *Introduction to dislocations*. Butterworth, Heinemann, 4th edition edition, 2001.

[150] J. P. Hirth and J. Lothe. *Theory of dislocations*. Krieger, Malabar, Florida, 2nd edition, 1992.

[151] S. P. Fitzgerald and S. Aubry. Self-force on dislocation segments in anisotropic crystals. *Journal of physics-condensed matter*, 22(29), 2010.

[152] S. P. Fitzgerald, S. Aubry, S. L. Dudarev, and W. Cai. Dislocation dynamics simulation of Frank-Read sources in anisotropic alpha-Fe. *Modelling and simulation in materials science and engineering*, 20(4), 2012.

[153] T. Diaz de la Rubia, H. M. Zbib, T. A. Khraishi, B. D. Wirth, M. Victoria, and M. J. Caturla. Multiscale modelling of plastic flow localization in irradiated materials. *Nature*, 406:871–874, 2000.

[154] Yu. N. Osetsky, A. Serra, and V. Priego. Interactions between interstitial clusters in fe and cu. *J. Nucl. Mater.*, 276:202–212, 200.

[155] M. A. Puigvi, N. de Diego, A. Serra, Yu. N. Osetsky, and D. J. Bacon. On the interaction between a vacancy and self-interstitial atom clusters in metals. *Phil. Mag.*, 87(23):3501, 2007.

[156] D. Mordehai, M. Fivel E. Clouetab, and M. Verdier. Introducing dislocation climb by bulk diffusion in discrete dislocation dynamics. *Phil. Mag. A*, 88(6):899–925, 2008.

[157] D. Terentyev, M. Klimenkov, and L. Malerba. Confinement of motion of interstitial clusters and dislocation loops in BCC Fe-Cr alloys. *J. Nucl. Mater.*, 393(1):30–35, 2009.

[158] H. Eyring. *J. Chem. Phys.*, 3:107, 1935.

[159] E. Wigner. *Z. Phys. Chem. Abt.*, 19:203, 1932.

[160] A. Brailsford and R. Bullough. *R. Philos. Trans. R. Soc. London*, 302:87, 1981.

[161] N. Doan and G. Martin. *Physical Review*, 67:134107, 2003.

[162] J. N. Reddy. *An Introduction to the Finite Element Method*. McGraw-Hill, third edition, 2005.

[163] R. Deborst and H. B. Muhlhaus. Gradient-dependent plasticity - formulation and algorithmic aspects. *Int. J. Num. Methods in Engr.*, 35(3):521, 1992.

[164] S. Kohlhoff, P. Gumbsch, and H. F. Fischmeister. Crack propagation in b.c.c. crystals studied with a combined finite-element and atomistic model. *Phil. Mag A*, 64:851, 1991.

[165] E. B. Tadmor, M. Ortiz, and R. Phillips. Quasicontinuum analysis of defects in solids. *Phil. Mag. A*, 73(6):1529, 1996.

[166] V. B. Shenoy, R. Miller, E. B. Tadmor, R. Phillips, and M. Ortiz. Quasicontinuum models of interfacial

structure and deformation. *Phys. Rev. Lett.*, 80(4):742, 1998.

[167] K. Masaki, K. Kodama, T. Ando, M. Saidoh, M. Shimizu, T. Hayashi, and K. Okuno. Tritium retention in graphite inner wall of jt-60u. *Fusion Engineering and Design*, 31(2):181 – 187, 1996.

[168] The Max-Planck Institute for Plasma Physics web pages 21.1.2014, http://www.ipp.mpg.de/ippcms/eng/for/projekte/w7x/device/divertor/index.html.

[169] J. Roth, B. M. U. Scherzer, R. S. Blewer, D. K. Brice, S. T. Picraux, and W. R. Wampler. Trapping, detrapping and replacement of kev hydrogen implanted into graphite. *J. Nucl. Mater.*, 93 & 94:601–607, 1980.

[170] T. Yamashina and T. Hino. Plasma-surface interactions of graphite as nuclear fusion material. *Appl. Surf. Sci.*, 48/49:483–497, 1991.

[171] A. Horn, A. Schenk, J. Biener, B. Winter, C. Lutterloh, M. WIttmann, and J. Küppers. H atom impact induced chemical erosion reaction at c:h film surfaces. *Chem. Phys. Lett.*, 231:193–198, 1994.

[172] K. Nakamura, A. Nagase, M. Dairaku, M. Akiba, M. Araki, and Y. Okumura. Sputtering yields of carbon based materials under high particle flux with low energy. *J. Nucl. Mater.*, 220-222:890–894, 1995.

[173] J. Roth and C. García-Rosales. Analytic description of the chemical erosion of graphite by hydrogen ions. *Nuclear Fusion*, 36(12):1647–59, 1996. with corrigendum Nuclear Fusion **37**, 897 (1997).

[174] Masaki Tanihuchi, Kazuyoshi Sato, Koichiro Ezato, Kenji Yokoyama, Masayuki Dairaku, and Masato Akiba. Sputtering of carbon-tungsten mixed materials by low energy deuterium. *J. Nucl. Mater.*, 313-316:360–363, 2003.

[175] C. Hopf, A. von Keudell, and W. Jacob. Chemical sputtering of hydrocarbon films. *J. Appl. Phys.*, 94(4):2373, 2003.

[176] F. W. Meyer, H. F. Krause, and L. I. Vergara. Measurements of chemical erosion of atj graphite by low energy $d_2^+$ impact. *J. Nucl. Mater.*, 337-339:922, 2005.

[177] J. Roth. Chemical sputtering. In R. Behrisch, editor, *Sputtering by Particle bombardment*, volume I, pages 91–146. Springer, Berlin, 1981.

[178] E. de Juan Pardo, M. Balden, B. Cieciwa, C. Garcia-Rosales, and J. Roth. Erosion processes of carbon materials under hydrogen bombardment and their mitigation b. *Physica Scripta*, T111:62–67, 2004.

[179] K. Nordlund, E. Salonen, J. Keinonen, and C. H. Wu. Sputtering of hydrocarbons by ion-induced breaking of chemical bonds. *Nucl. Instr. Meth. Phys. Res. B*, 180:77, 2000.

[180] E. Salonen, K. Nordlund, J. Keinonen, N. Runeberg, and C. H. Wu. Reduced chemical sputtering of carbon by silicon doping. *J. Appl. Phys.*, 92:2216–2218, 2002.

[181] P. Träskelin, K. Nordlund, and J. Keinonen. H, he, ne, ar-bombardment of amorphous hydrocarbon structures. *J. Nucl. Mater*, 357:1–8, 2006.

[182] E. D. de Rooij, U. von Toussaint, A. W. Kleyn, and W. J. Goedheer. Molecular dynamics simulations of amorphous hydrogenated carbon under high hydrogen fluxes. *Phys. Chem. Chem. Phys.*, 11(42):9823, 2009.

[183] C. O. Reinhold, P. S. Krstic, S. J. Stuart, H. Zhang, P. R. Harris, and F. W. Meyer. Isotope dependence of chemical erosion of carbon. *J. Nucl. Mater.*, 401:1–12, 2010.

[184] V. Kh. Alimov, D. B. Bogomolov, M. N. Churaeva, A. E. Gorodetsky, S. L. Kanashenko, A. I. Kanaev, S. Yu. Rybakov, V. M. Sharapov, A. P. Zakharov, R. Kh. Zalavutdinov, O. I. Buzhinsky, A. P. Hernobay and. S. A. Grashin, S. V. Mirnov, V. I. Bregadze, and A. Yu. Usyatinsky. Characterization of a-b/c:h films deposited from different boron containing precursors. *J. Nucl. Mater.*, 196-198:670–675, 1992.

[185] B. A. Kalin, V. L. Yakushin, V. I. Polsky, and Yu. S. Virgilev. Sputtering of surface-boronized graphite by hydrogen ion bombardment. *J. Nucl. Mater.*, 212-215:1206–1210, 1994.

[186] C. H. Wu, C. Alessandrini, R. Moormann, M. Rubel, and B. M. U. Scherzer. Evaluation of silicon doped cfcs for plasma facing material. *J. Nucl. Mater*, 220-222:860–864, 1995.

[187] C. H. Wu, C. Alessandrini, P. Bonal, A. Caso, H. Grote, R. Moormann, A. Perujo, M. Balden, H. Werle, and G. Vieider. Evaluation of an advanced silicon doped cfc for plasma facing material. In C. Varandas and F. Serra, editors, *Fusion Technology 1996*, pages 327–330. Elsevier Science B.V., Amsterdam, the Netherlands, 1997.

[188] M. Balden, J. Roth, and C. H. Wu. Thermal stability and chemical erosion of the silicon doped cfc

material ns31. *J. Nucl. Mater.*, 258-263:740–744, 1998.

[189] H. Grote, W. Bohmeyer, P. Kornejew, H.-D. Reiner, G. Fussmann, R. Schlögl, G. Weinberg, and C. H. Wu. Chemical sputtering yields of carbon based materials at high ion flux densities. *J. Nucl. Mater.*, 266-269:1059–1064, 1999.

[190] E. Salonen, K. Nordlund, J. Keinonen, and C. H. Wu. Chemical sputtering of amorphous silicon carbide under hydrogen bombardment. *Applied Surface Science*, 184:387–390, 2001.

[191] S. Brezinsek, S. Jachmich, M. F. Stamp, A.G. Meigs, J.W. Coenen, K. Krieger, C. Giroud, M. Groth, V. Philipps, S. GrÃ$\frac{1}{4}$nhagen, R. Smith, G. J. van Rooij, D. Ivanova, G. F. Matthews, and JET-EFDA Contributors. Residual carbon content in the initial iter-like wall experiments at jet. *J. Nucl. Mater.*, 438:S703, 2013.

[192] K. Nordlund, E. Salonen, A. V. Krasheninnikov, and J. Keinonen. Swift chemical sputtering of covalently bonded materials. *Pure and Applied Chemistry*, 78(6):1203–1212, 2006.

[193] K. Nordlund, C. Björkas, K. Vörtler, A. Meinander, A. Lasa, M. Mehine, and A. V. Krasheninnikov. Mechanism of swift chemical sputtering: comparison of be/c/w dimer bond breaking. *Nucl. Instr. Meth. Phys. Res. B*, 269(11):1257–1261, 2011.

[194] C. Björkas, D. Borodin, A. Kirschner, R. K. Janev, D. Nishijima, R. Doerner, and K. Nordlund. Molecules can be sputtered also from pure metals: sputtering of beryllium hydride by fusion plasma-wall interactions. *Plasma Physics and Controlled Fusion*, 55:074004, 2012.

[195] A. Lasa, C. Björkas, K. Vörtler, and K. Nordlund. Md simulations of low energy deuterium irradiation on w, wc andw2c surfaces. *J. Nucl. Mater.*, 429:284–292, 2012.

[196] C. Björkas and K. Nordlund. Variables affecting simulated be sputtering yields. *J. Nucl. Mater.*, 439:174–179, 2013.

[197] C Björkas, K. Vörtler, K. Nordlund, D. Nishijima, and R. Doerner. Chemical sputtering of be due to d bombardment. *New J. Phys.*, 11:123017, 2009.

[198] D. Nishijima, R. P. Doerner, M. J. Baldwin, G. De Temmerman, and E. M. Hollmann. Properties of bed molecules in edge plasma relevant conditions. *Plasma Phys. Control. Fusion*, 50:125007, 2008.

[199] G. Duxbury, M. F. Stamp, and H.P. Summers. Observations and modelling of diatomic molecular spectra from jet. *Plasma Phys. Control. Fusion*, 40:361, 1998.

[200] S. Brezinsek. 2013. EPS conference 2013.

[201] A. Kirschner, P. Wienhold, V. Phillips, J.P. Coad, A. Huber, U. Samm, and JET EFDA contributors. Modelling of carbon transport in fusion devices: evidence of enhanced re-erosion of in-situ re-deposited carbon. *Journal of Nuclear Materials*, 328:62, 2004.

[202] C. Björkas, D. Borodin, A. Kirschner, R. K. Janev, D. Nishijima, R. Doerner, and K. Nordlund. Multi-scale modeling of bed release and transport in pisces-b. *J. Nucl. Mater.*, 438:S276–S279, 2012.

[203] J. Luthin and Ch. Linsmeier. Carbon films and carbide formation on tungsten. *Surface Science*, 454-456:78–82, 2000.

[204] Ch. Linsmeier, J. Luthin, and P. Goldstrass. Mixed material formation and erosion. *J. Nucl. Mater.*, 290-293:25–32, 2001.

[205] K. Inai, Y. Kikuhara, and K. Ohya. Comparison of carbon deposition on tungsten between molecular dynamics and dynamic monte carlo simulation. *Surface and Coatings Technology*, 202:5374–5378, 2008.

[206] P. Träskelin, C. Björkas, N. Juslin, K. Vörtler, and K. Nordlund. Radiation damage in wc studied with md simulations. *Nucl. Instr. Meth. Phys. Res. B*, 257:614, 2007.

[207] P. Träskelin, N. Juslin, P. Erhart, and K. Nordlund. Molecular dynamics simulations of hydrogen bombardment of tungsten carbide surfaces. *Physical review B*, 75:174113, 2007.

[208] K. Vörtler, C. Björkas, and K. Nordlund. The effect of plasma impurities on the sputtering of tungsten carbide. *J. Phys.: Conden. Matter*, 23(8):085002, 2010.

[209] C. Björkas, K. Vörtler, and K. Nordlund. Major elemental assymetry and recombination effects in irradiated wc. *Phys. Rev. B (Rapid comm.)*, 74:140103, 2006.

[210] G. Petzow, F. Aldinger, S. Jonsson, and O. Preuss. *Ullmanns Encyclopedia of Industrial Chemistry*, volume A4, chapter Beryllium and Beryllium Compounds, page 11. X, 1985.

[211] P. Goldstrass and Ch. Linsmeier. Formation of mixed layers and compounds on beryllium due to c and co bombardment. *Journal of Nuclear Materials*, 290-293:71–75, 2001.

[212] Yves Ferro, Alain Allouche, and Christian Linsmeier. Absorption and diffusion of beryllium in graphite, beryllium carbide formation investigated by density functional theory. *Journal of Applied Physics*, 113(21):213514, 2013.

[213] Chaofeng Sang, Xavier Bonnin, Manoj Warrier, Abha Rai, Ralf Schneider, Jizhong Sun, and Dezhen Wang. Modelling of hydrogen isotope inventory in mixed materials including porous deposited layers in fusion devices. *Nuclear Fusion*, 52(4):043003, 2012.

[214] Joachim Roth. Chemical erosion of carbon based materials in fusion devices. *Journal of Nuclear Materials*, 266-269:51 – 57, 1999.

[215] K. Balasubramanian. Spectroscopic constants and potential energy curves of tungsten carbide. *J. Chem. Phys.*, 112(17):7425, 2000.

[216] A. Meinander, C. Björkas, and K. Nordlund. The effect of hydrocarbon chemistry on sputtering in mixed be-c-h materials. *Nucl. Instr. Meth. Phys. Res. B*, 303:188, 2013.

[217] K. Heinola, T. Ahlgren, E. Vainonen-Ahlgren, J. Likonen, and J. Keinonen. *Physica scripta T*, 128:91, 2007.

[218] T. Ahlgren, K. Heinola, K. Vörtler, and J. Keinonen. *J. Nucl. Mater.*, 427:152, 2012.

[219] V. K. Alimov, J. Roth, R. Causey, D. Komarov, C. Linsmeier, A. Wiltner, F. Kost, and S. Lindig. *J. Nucl. Mater.*, 375:192, 2008.

[220] H.-B. Zhou, Y.-L. Liu, S. Jin, and Y. Zhang. *Nucl. Fusion*, 50:025016, 2010.

[221] A. Haasz, M. Poon, R. Macaulay-Newcombe, and J. Davis. *J. Nucl. Mater.*, 290, 2001.

[222] T. Matsui, S. Muto, and T. Tanabe. *J. Nucl. Mater.*, 283, 2000.

[223] R. Sakamoto, T. Muroga, and N. Yoshida. Microstructural evolution induced by low energy hydrogen ion irradiation in tungsten. 220-222(0):819 – 822, 1995.

[224] C. García-Rosales, P. Franzen, H. Plank, J. Roth, and E. Gauthier. Re-emission and thermal desorption of deuterium from plasma sprayed tungsten coatings for application in asdex-upgrade. 233–237:803 – 808, 1996.

[225] A. A. Pisarev, I. D. Voskresensky, and S. I. Porfirev. Computer modeling of ion implanted deuterium release from tungsten. 313–316:604, 2003.

[226] G.M. Wright, D. Brunner, M.J. Baldwin, R.P. Doerner, B. Labombard, B. Lipschultz, J.L. Terry, and D.G. Whyte. Tungsten nano-tendril growth in the alcator c-mod divertor. *Nuclear Fusion*, 52(4):042003, 2012.

[227] Shin Kajita, Wataru Sakaguchi, Noriyasu Ohno, Naoaki Yoshida, and Tsubasa Saeki. Formation process of tungsten nanostructure by the exposure to helium plasma under fusion relevant plasma conditions. *Nuclear Fusion*, 49(9):095005, 2009.

[228] M.J. Baldwin, T.C. Lynch, R.P. Doerner, and J.H. Yu. Nanostructure formation on tungsten exposed to low-pressure rf helium plasmas: A study of ion energy threshold and early stage growth. *J. Nucl. Mater.*, 415(1, Supplement):S104 – S107, 2011.

[229] M.J. Baldwin, R.P. Doerner, D. Nishijima, K. Tokunaga, and Y. Ueda. The effects of high fluence mixed-species (deuterium, helium, beryllium) plasma interactions with tungsten. *J. Nucl. Mater.*, 390-391(0):886 – 890, 2009.

[230] S. I. Krasheninnikov. Viscoelastic model of tungsten 'fuzz' growth. *Phys. Scr.*, T145:014040, 2011.

[231] Shahram Sharafat, Akiyuki Takahashi, Koji Nagasawa, and Nasr Ghoniem. A description of stress driven bubble growth of helium implanted tungsten. *J. Nucl. Mater.*, 389(2):203 – 212, 2009.

[232] Yu.V. Martynenko and M. Yu. Nagel. Model of fuzz formation on a tungsten surface. *Plasma Physics Reports*, 38(12):996–999, 2012.

[233] A. Lasa, S. K. Tähtinen, and K. Nordlund. Loop punching and bubble rupture causing surface roughening - a model for w fuzz growth. *EPL*, 105:25002, 2014.

[234] M.J. Baldwin and R.P. Doerner. Formation of helium induced nanostructure 'fuzz' on various tungsten grades. *J. Nucl. Mater.*, 404(3):165 – 173, 2010.

[235] C.S. Becquart, A. Souidi, C. Domain, M. Hou, L. Malerba, and R. E. Stoller. Effect of displacement

cascade structure and defect mobility on the growth of point defect clusters under irradiation. *Journal of Nuclear Materials*, 351:39, 2006.

[236] C.S. Becquart and C. Domain. Ab initio calculations about intrinsic point defects and he in w. *Nuclear Instruments and Methods in Physics Research Section B: Beam Interactions with Materials and Atoms*, 255(1):23 – 26, 2007.

[237] C.S. Becquart and C. Domain. A density functional theory assessment of the clustering behaviour of he and h in tungsten. *J. Nucl. Mater.*, 386-388(0):109 – 111, 2009.

[238] C.S. Becquart and C. Domain. An object kinetic monte carlo simulation of the dynamics of helium and point defects in tungsten. *J. Nucl. Mater.*, 385(2):223 – 227, 2009.